Materials & Design 242 (2024) 112996

Contents lists available at ScienceDirect

Materials & Design

journal homepage: www.elsevier.com/locate/matdes

Synergistic effects of Monel 400 filler wire in gas metal arc welding of CoCrFeMnNi high entropy alloy

Jiajia Shen [a,f,*], Yeon Taek Choi [b], Rita Gonçalves [a], Norbert Schell [c], Jin Yang [d], Zhi Zeng [e], Ana Catarina Baptista [f], Hyoung Seop Kim [b], J.P. Oliveira [a,f,*]

[a] UNIDEMI, Department of Mechanical and Industrial Engineering, NOVA School of Science and Technology, Universidade NOVA de Lisboa, 2829-516 Caparica, Portugal
[b] Graduate Institute of Ferrous Technology, POSTECH (Pohang University of Science and Technology), Pohang 790-794, South Korea
[c] Helmholtz-Zentrum Hereon, Institute of Materials Physics, Max-Planck-Str. 1, Geesthacht 21502, Germany
[d] School of Materials Engineering, Shanghai University of Engineering Science, Shanghai 201620, China
[e] School of Mechanical and Electrical Engineering, University of Electronic Science and Technology of China, Sichuan 611731, China
[f] CENIMAT/I3N, Department of Materials Science, NOVA School of Science and Technology, Universidade NOVA de Lisboa, 2829-516 Caparica, Portugal

ARTICLE INFO

Keywords:
CoCrFeMnNi high entropy alloy
Monel NiCu-7 filler wire
Gas metal arc welding
Digital image correlation
Thermodynamic calculations
Mechanical testing

ABSTRACT

Weldability plays a crucial role in the journey of high entropy alloys towards their engineering applications. In this study, gas metal arc welding was performed to join an as-rolled CoCrFeMnNi high entropy alloy using Monel 400 as the filler wire. The present research findings demonstrate a favorable metallurgical chemical reaction between the Monel 400 filler and the CoCrFeMnNi high entropy alloy, resulting in compositional mixing within the fusion zone that promotes a solid-solution strengthening effect, counteracting the typical low hardness associated to the fusion zone of these alloys. The weld thermal cycle induced multiple microstructure changes across the joint, including variations in the grain size, existing phases and local texture. The grain size was seen to increase from the base material toward the fusion zone. An FCC matrix and finely sparse Cr-Mn-based oxides existed in both base material and heat affected zone, while in the fusion zone new FCC phases and carbides were formed upon the mixing of the Monel 400 filler. The role of the filler material on the fusion zone microstructure evolution was rationalized using thermodynamic calculations. Texture shifted from a γ-fiber (in the base material) to a strong cubic texture in the fusion zone. Digital image correlation during tensile testing to fracture coupled with microhardness mapping revealed that, stemming from the process-induced microstructure changes, the micro and macromechanical response differed significantly from the original base material. This study successfully established a correlation between the impact of the process on the developed microstructural features and the resultant mechanical behavior, effectively assessing the processing-microstructure-properties relationships towards an improved understanding of the physical metallurgy associated to these advanced engineering alloys. In conclusion, this work provides an important theoretical framework and practical guidance for optimizing the engineering applications of high entropy alloys.

1. Introduction

In recent years, the emergence of high entropy alloys (HEAs) has captured significant attention within the field of metallic materials [1,2]. Their distinct design concept imparts excellent corrosion and wear resistance [3–7], as well as remarkable mechanical properties over a wide temperature range [8,9], positioning them as materials with substantial potential for critical applications in advanced industries. Of these alloys, the equiatomic CoCrFeMnNi HEA has received the most extensive research, distinguished by its single FCC structure and remarkable mechanical properties. [10]. Such inherent characteristics position these materials as promising contenders for fulfilling structural roles across diverse engineering applications.

To ensure the feasibility of utilizing these alloys in complex structural configurations, their weldability is a crucial issue that needs to be addressed. It is known that any advanced engineering alloy requires welding to enable complex structural shapes to exist. Therefore, evaluating the weldability of these novel alloys is essential to further expand

* Corresponding authors.
E-mail addresses: j.shen@fct.unl.pt (J. Shen), jp.oliveira@fct.unl.pt (J.P. Oliveira).

https://doi.org/10.1016/j.matdes.2024.112996
Received 26 March 2024; Received in revised form 30 April 2024; Accepted 2 May 2024
Available online 3 May 2024

their potential application areas. Fusion welding processes, based on rapid melting and solidification, are currently the most mature in industry. The welding process will impact both the microstructure changes, as well as their extension. For example, laser welding is widely used for advanced materials joining due to the reduced heat source dimensions, but the high initial capital investment required for this technique may hinder its application in industry. In contrast, fusion-based welding technologies based on the electrical arc are perceived as a cost-effective alternative that can achieve sound joints with good mechanical properties in various engineering alloys.

Fusion-based welded joints typically exhibit three distinct regions: the base material (BM), which remains unchanged throughout the whole welding process, and is used as benchmark to evaluate the impact of the process thermal cycle across the joint; the heat affected zone (HAZ), where the weld thermal cycle promotes a temperature increase, without reaching full melting, allowing for solid-state transformations to occur; and the fusion zone (FZ), where the material undergoes full melting and subsequent rapid and non-equilibrium solidification. A notable issue in fusion-based welded joints is the easy formation of coarse columnar grains within the FZ [11]. According to the Hall-Petch equation [12] this will lower the yield strength of the deposited material, consequently diminishing its mechanical resistance. However, one potential solution to address this challenge is the introduction of a filler wire into the FZ during the welding process. This approach serves a dual purpose: adjusting the chemical composition to regulate the microstructure features, by potentially changing the solidification path and formed phases, or to promote solid solution strengthening allowing for the use of the joint in critical-related applications. However, the inappropriate addition of filler metal to the FZ can result in non-uniform chemical composition within the weld metal. This can lead to the formation of detrimental phases and promote crack propagation. Even so, dissimilar joints remain a preferred choice as they offer design flexibility and performance enhancements. Therefore, comprehensively understanding the microstructural evolution and mechanical behavior of dissimilar joints involving HEAs is of paramount importance.

From the available literature review [13–15], it is evident that welding of HEAs has been gaining increasing attention, although it is still at an early stage. When it comes to CoCrFeMnNi HEAs, a considerable number of studies have confirmed their good weldability [16–23], especially in similar combinations. Thereby, focus should now be steered on exploring and developing specific filler materials to regulate the performance of CoCrFeMnNi welded joints. Regarding this topic, only three types of filler wires for welding CoCrFeMnNi HEAs have been investigated to date, including 304 [24,25], 308 [26,27] and 410 stainless steels [28]. The aforementioned studies have all reported achieving sound dissimilar welded joints. Nevertheless, research in this area remains limited, especially considering the abundance of potentially available filler materials, which are widely used for joining conventional engineering alloys as steels or Ni-based alloys.

In this study, Monel 400 was selected as the filler wire considering both performance and costs. Firstly, given the high cost of CoCrFeMnNi HEA due to its unique properties, using Monel 400 as the filler wire can reduce the usage of other expensive alloys to some extent, thereby achieving cost control. Secondly, Monel 400 stands out for its excellent corrosion resistance and high strength [29–31]. By optimizing welding processes and parameters, it is expected that the advantages of Monel 400 filler wires can be utilised to improve the overall tensile strength, yield strength and impact resistance of the joints. Therefore, the selection of Monel 400 as the filler wire is based on a combination of superior performance and cost-effectiveness, aiming to achieve efficient and reliable welding processes to meet the demanding requirements of engineering applications.

In past studies, while filler wires such as 304, 308, and 410 stainless steels have made some progress in welding CoCrFeMnNi HEA, there have been limitations, particularly in terms of mechanical stability and corrosion resistance in high temperature environments. The use of Monel 400, as a filler wire, presents a potential solution to these limitations. Its outstanding high temperature stability and corrosion resistance are expected to effectively overcome the previous limitations of already used filler wires. This advancement is poised to facilitate the widespread application of HEAs in extreme environments. Additionally, it is worth noting that there are currently no literature reports on the use of Ni-based welding wires for gas metal arc welding of CoCrFeMnNi HEAs. This means that Monel 400, as a Ni-based high temperature alloy, holds potential for innovation and application in this field. By adopting Monel 400 as the filler wire, it is expected to fill this gap in the field and provide new solutions for the welding of CoCrFeMnNi HEAs.

This study comprehensively examines the effects of gas metal arc welding on a CoCrFeMnNi alloy, utilizing Monel 400 as the filler wire. The approach integrates microstructural characterization techniques with mechanical property assessment methods, aiming to establish correlations among processing, microstructural features, and mechanical properties. Further supported by thermodynamic calculations, e.g. reproduction of non-equilibrium solidification paths in the weld pool, simulating phase formation sequences and potential formation of precipitated phases, as well as elemental redistribution and segregation during solidification, thus bridging the gap in the existing body of knowledge. Within this background, the study places particular emphasis on comprehending the influence of the weld thermal cycle on microstructure evolution, and the subsequent impact of these changes on the resultant mechanical properties. To achieve this, optical and electron microscopy, high energy synchrotron X-ray diffraction, and thermodynamic simulations were used to evaluate the microstructure evolution, while microhardness testing and uniaxial tensile tests coupled with Digital Image Correlation (DIC) analysis are employed to quantitatively evaluate the mechanical properties of the welded joints. The core focus of the present study lies in two key aspects: firstly, to explore the interaction between the grain refinement induced by previous cold rolling of the BM and the subsequent thermal cycle during welding, and how these impacts the material at the microstructural level, including grain growth, recrystallization processes, solid-state phase transformation mechanisms, and texture evolution in the HAZ and FZ. Secondly, the work aims to conduct a detailed analysis on how factors such as grain size, existing phases and distributions, and texture evolution, impact the distribution of material hardness, as well as the influence on the local and macroscopic mechanical properties of the welded joint, aiming to comprehensively elucidate the intrinsic connections and mutual influence mechanisms between microstructural characteristics and resultant mechanical properties. The ultimate goal is to provide valuable insights for researchers in the materials engineering domain, aiding in understanding the metallurgical reactions between CoCrFeMnNi and the selected Monel 400 filler wire.

2. Experimental procedures

2.1. Materials

In this study, vacuum-induced melting was employed to prepare an as-cast equiatomic CoCrFeMnNi HEA with a thickness of 3 mm. The detailed preparation methodology is given in reference [32]. Then, cold rolling was used to reduce the material thickness to 1.5 mm for subsequent welding experiments, where 45 × 45 mm squares were used for butt joining. It is worth noting that during the cold rolling process to reduce the thickness from 3 mm to 1.5 mm, the CoCrFeMnNi HEA experiences multiple rolling passes gradually thinning. Each pass applies the same pressure along the same rolling direction, compressing and elongating the material in the desired direction and ensuring uniform deformation along the desired axis. Several potential factors to consider in this process include material deformation and uniformity, rolling mill pressure/direction and temperature control, surface quality and flatness, as well as process control and equipment adjustments, all of which are crucial for ensuring the overall uniformity of the material after

rolling. The BM composition is detailed in Table 1. Prior to welding, the edges of the joints were polished to ensure good contact. Acetone and alcohol were utilized combined to polishing and cleaning to thoroughly eliminate contaminants that might compromise the integrity of the welded joints. These pre-welding treatments are crucial to ensure the quality and performance of the welded joints, they also play a vital role in minimizing potential disruptive factors during the process.

2.2. Gas metal arc welding

For gas metal arc welding, a Bester 215MP model Welding Machine from Lincoln Electric was used. Monel 400 was selected as the filler wire, and its composition is depicted in Table 2. The welding parameters utilized included a voltage of 16 V, a torch travel speed of 170 mm/min, and a wire feed speed of 2000 mm/min. Based on the calculation, the heat input, HI, defined as the power to welding speed ration weighted by the thermal efficiency of the process, is 338.86 J/mm. Here, the thermal efficiency is approximately ≈0.4, based on empirical data for gas metal arc welding [33]. This parameter considers energy losses due to gas ionization, the surrounding environment, and filler material (if present), providing a more accurate reflection of energy transfer during the welding process. This heat input directly influences the peak temperature and duration of high temperatures during welding, critical factors that affect microstructure and mechanical properties. Specifically, the weld thermal cycles significantly impact grain size, phase distribution, and the likelihood of defect formation, ultimately determining the performance of the welded joint. Throughout the entire welding process, 99.99 % pure Ar shielding gas was utilized to prevent oxidation of the FZ and its surroundings. For optimal efficacy, the shielding gas was channeled into two different routes. One channel was in the welding torch nozzle, while another one was directed to the root of the joint. As a result, the welding bead had both top and bottom sides protected by the Ar shielding gas. After welding, dog-bone shaped samples were obtained by electrical discharge machining. These samples were then used for microstructural characterization and mechanical testing. It is worth noting that in this study, the selection of welding parameters was not arbitrary or isolated, but based on extensive prior experimentation and data analysis. Besides, the basis of welding parameters selection is to achieve full penetration, defect-free, and high-strength weld joints using minimal heat input, to meet the specific requirements for welding CoCrFeMnNi HEA with Monel 400 filler wire. However, this study did not cover the effects of different parameter combinations on the quality and performance of the joints, which will be a focus of future research.

2.3. Microstructure characterization

Standard metallographic preparation techniques were employed to prepare the welded joints for microstructure characterization. Initially, the dog-bone shaped welded joints were embedded in epoxy resin, in this process, a cold embedding epoxy resin is utilized, with both the resin and hardener in liquid form. At ambient temperature, the resin and hardener are combined at a 4:1 ratio, then carefully poured into a rubber container containing the samples. After a 6-hour period, the mixture cures into a transparent, rigid material. Following this, a stepwise polishing and grinding process was carried out using SiC papers with varying degrees of roughness, such as 240, 320, 400, 600, 800, 1200, 2500 and 4000 grit. And eventually, a polishing cloth and 2 μm diamond polishing paste are employed until a mirror-like surface was obtained. Afterwards, a solution of aqua regia (5 ml HNO_3 and 15 ml HCl) was used for etching the samples to expose the microstructure of the joints. Optical microscopy observations were conducted using a Leica DMI 5000 M inverted optical microscope. For electron microscopy examinations, a JEOL JSM-7800F PRIME high-resolution field emission scanning electron microscope (SEM) equipped with dual-energy dispersive X-ray diffraction (EDS). Electron backscatter diffraction analysis (EBSD) was performed using a FEI SL-30S 46FEG SEM to obtain crystallographic information across the welded samples. The raw EBSD data was processed using TSL OIM Analysis 7.2 software.

To gain a deeper insight into the microstructural characteristics of the welded joints, further microstructural characterization was conducted using high-energy synchrotron X-ray diffraction. These measurements were performed at the P07B beamline of PETRA III/DESY in Hamburg, Germany. The applied wavelength was set to 0.14235 Å, corresponding to a beam energy of 87.1 kV, and the distance from the sample to the detector was approximately 1.306 m. This experimental setup allowed for scanning the material in transmission mode to determine bulk microstructural information from the welded joint. A square beam spot with dimensions of 200 × 200 μm^2 was used to probe the sample, with an incremental step size of 200 μm between consecutive analyzed points. The measurements were initiated in the BM region, traversed through the HAZ, FZ, and continued until reaching the BM at the other end of the joint. This strategy ensured coverage of the entire welded material. For capturing the Debye-Scherrer rings, a 2D PerkinElmer detector was utilized to record the resulting diffraction data. Subsequent processing of the acquired synchrotron raw data was performed using in-house Python scripts in conjunction with MAUD (Materials Analysis Using Diffraction) software.

To predict the non-equilibrium solidification process within the FZ during welding, thermodynamic calculations based on the Scheil-Gulliver model were performed using Thermo-Calc 2022a software along with TCHEA 5.1 database. These calculations encompassed the prediction of the solidification path and associated phase formation. Considering the presence of carbon (C) in the Monel 400 filer wire, this specific element was selected as a fast diffuser for the simulation process. Furthermore, the Scheil-Gulliver model is a method for predicting solute redistribution in multi-component systems by employing the "non-equilibrium lever rule", aiding in the prediction of segregation behavior of the primary components. Three fundamental assumptions are used in the Scheil-Gulliver model: no back diffusion in the solid phase; infinite diffusion in the liquid phase; and equilibrium at the solid–liquid interface.

2.4. Microhardness and mechanical testing

To explore the influence of varying microstructures across the joint on mechanical properties, microhardness measurements and uniaxial tensile tests were conducted. A Mitutoyo HM-112 micro-Vickers hardness tester was used with a load of 0.5 kg applying continuous loading for 10 s at each measurement point. The microhardness measurements initiated from the BM region on one side of the welded joint, passing through the HAZ and FZ, and finished at the opposite side of the BM. The interval between longitudinal and transverse indents was maintained at 50 μm. Uniaxial tensile tests were performed on a Shimadzu machine with a maximum load capacity of 50 kN. These tests were executed at room temperature, maintaining a constant strain rate of 1×10^{-3} s^{-1}, with the tensile direction perpendicular to the weld, until failure occurred. Here, the gauge length, width, and thickness of the dog-bone-shaped sample used for tensile testing are 27.7 mm, 1.5 mm, and 1.5 mm

Table 1
Nominal Composition of the as-rolled CoCrFeMnNi BM (at. % / wt.%).

	Co	Cr	Fe	Mn	Ni
at. %	20.00	20.00	20.00	20.00	20.00
wt. %	21.02	18.53	19.92	19.59	20.93

Table 2
Nominal Composition of the Monel 400 filler wire (at. % / wt.%).

	Ni	Cu	Fe	Mn	Si	C
at. %	66.90	28.36	2.25	1.16	0.85	0.46
wt. %	66.02	30.30	2.11	1.07	0.40	0.10

respectively. Furthermore, digital image correlation (DIC) was utilized to monitor the localized deformation response in various regions of the welded joint, namely the BM, HAZ, and FZ, and three welded joints underwent repeated tensile tests under identical conditions to ensure the reproducibility of mechanical properties.

3. Results and discussions

3.1. Microstructure evolution

Fig. 1 provides an overview of the macro- and microstructural features of the as-welded CoCrFeMnNi HEA. From Fig. 1 a), the macroscopic cross-sectional view of the welded joint reveals a well-defined geometric shape with complete penetration, without any pores or cracks discernible. This serves as evidence that the CoCrFeMnNi/Monel 400 pair possesses a favorable and acceptable weldability for engineering applications. The FZ of this welded joint is a blend of the CoCrFeMnNi HEA and Monel 400 filler wire, underscoring a notable metallurgical interaction between these two materials. Interestingly, protrusions can be observed on both the upper and lower surfaces of the joint, which are defined as reinforcement. Regarding the formation of a reinforcement in on the surface and root of the weld, this is primarily due to the extra material coming from the filler wire during the welding process. The surface reinforcement is formed upon the addition of the molten filler wire and protrudes slightly as the wire moves forward during welding. The root reinforcement on the bottom surface of the joint is more obvious due to the surface tension of the melted wire during solidification [34]. These reinforcements can lead to the formation of weld toes, which are a form of geometric defect. When the joint undergoes deformation or loading, stress concentration is prone to occur in the weld toe region. This stress concentration increases the risk of crack initiation in the weld toe region, potentially leading to joint failure. This will be discussed in detail in the mechanical analysis section.

From the macrostructure of the welded joint (refer to Fig. 1 a)), distinct microstructural regions can be observed, delineating three typical regions of a fusion-based welded joint: BM, HAZ, and FZ. Corresponding high-magnification images are presented in Fig. 1 b), c), and e), respectively. With these high-magnification light optical microscope images, the differences in grain size and microstructural features become evident, which is related to the effect of the weld thermal cycle. Of particular interest, at the boundary between the HAZ and FZ (refer to Fig. 1 d)), a transition from small equiaxed and columnar grains to equiaxed dendritic growth is observed. Dendrites extend towards the centerline of the FZ, offering evidence of epitaxial growth (refer to Fig. 1 e-2)) [35,36]. This characteristic solidification microstructure, i.e., dendrites, pervades the entirety of FZ (refer to Fig. 1 e) and e-1)). This is attributed to the high cooling rate in this region, leading to rapid solidification. It should be noted that Fig. 1 presented here is intended solely to illustrate the microstructural morphology of various regions in the welded joint and does not involve quantitative analysis. Further quantitative analysis of microstructural features in different regions, such as grain size, dislocation density, and their evolution under the influence of weld thermal cycles, will be discussed in Fig. 2.

EBSD was employed to obtain a more detailed microstructural characterization of the welded joint. This technique, in conjunction with the cross-sectional view of the welded joint depicted in Fig. 1 a),

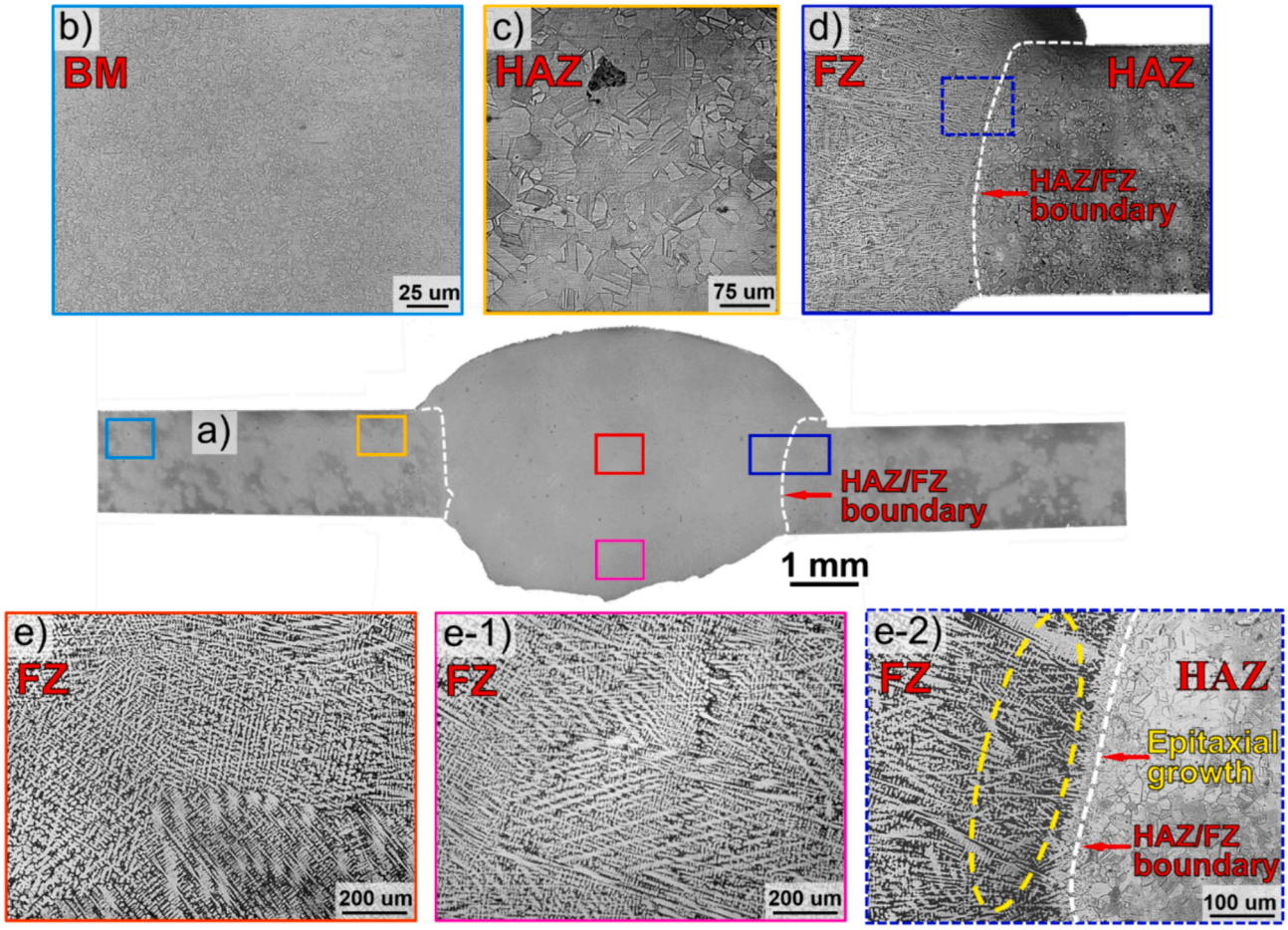

Fig. 1. Macro- and microstructural features of the as-welded HEA specimen: a) transverse cross-sectional view; b), c), d) and e)-e1) are close-up views of BM, HAZ, HAZ/FZ boundary and FZ, respectively.

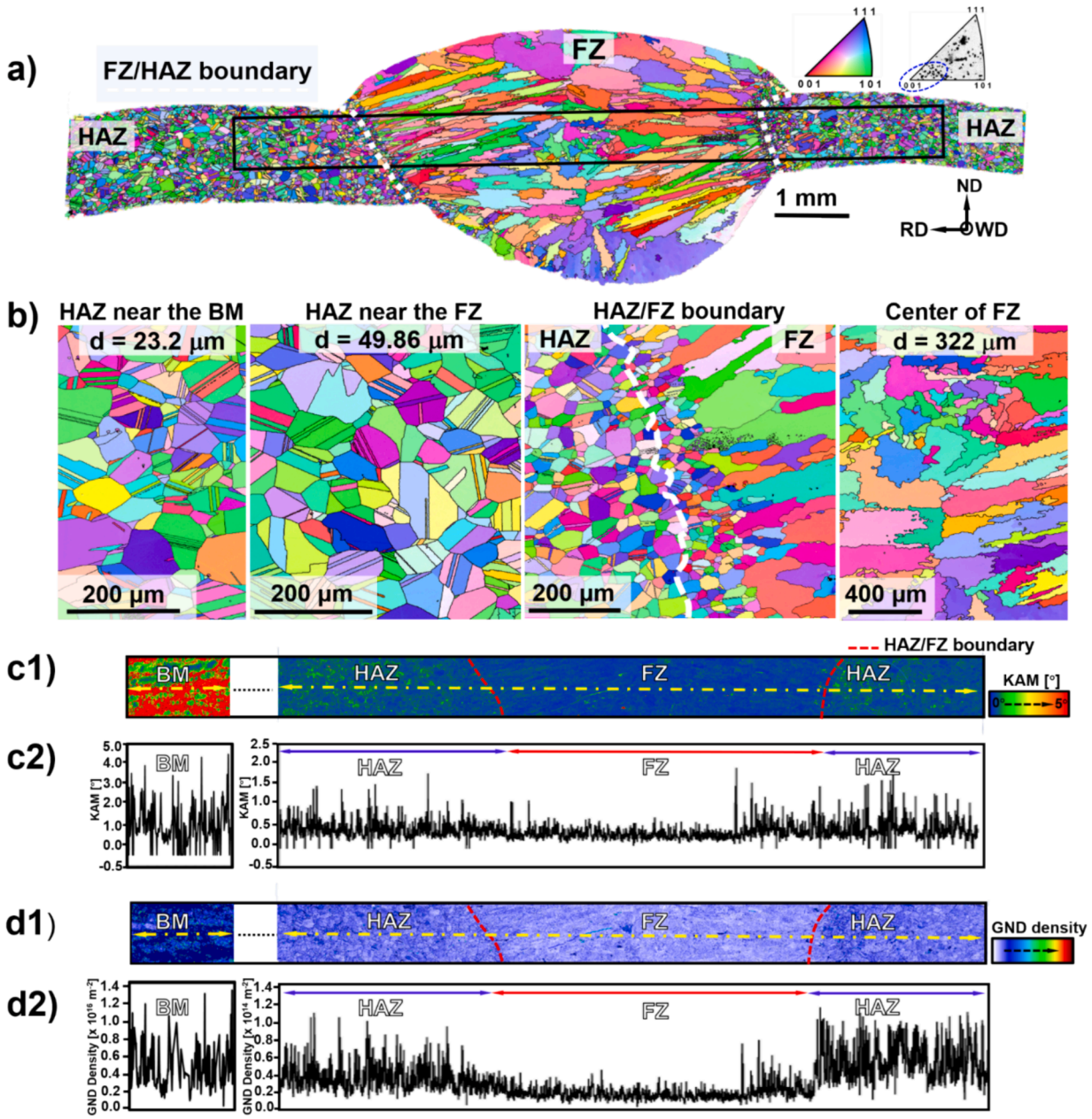

Fig. 2. a) EBSD analysis of the gas metal arc welded joint utilizing cocrfemnni alloy with monel 400 filler wire; b) IPF maps of the HAZ near the BM, HAZ near the FZ, HAZ/FZ boundary, and center of the FZ; c1) Kernel average misorientation (KAM) map; KAM values across the welded joint obtained along the yellow dashed line in c1); d1) Geometrically Necessary Dislocation (GND) density map; d2) GND values across the welded joint obtained along the yellow dashed line in d1). (For interpretation of the references to color in this figure legend, the reader is referred to the web version of this article.)

reconfirmed the defect-free nature of the obtained joints.

The microstructure of the present cold rolled BM has been discussed in a previous study [28], where the presence of thin pancake-like grains with a width of about ≈2 μm was found. In comparison to the BM, the HAZ experiences a phenomenon of grain coarsening (refer to Fig. 2 b)). The grain sizes in the HAZ near the BM and the HAZ near the FZ are approximately ≈23.2 and ≈49.86 μm, respectively. The driving forces behind these microstructural changes primarily originate from the weld thermal cycle and the pre-stored strain energy of the cold rolled BM. Specifically, the equiaxed grains observed in the HAZ are typical features of recrystallization. The weld thermal cycle induces effects in these two regions of the HAZ that resemble low- and high-temperature annealing, respectively, thereby releasing the pre-stored strain energy from the previous plastic deformation of the BM. This prompts solid state processes such as recovery, recrystallization, and grain growth to occur along the HAZ although their magnitude is dependent on the distance of the heat source. The noticeable differences in microstructural features between the HAZ and FZ make the boundary line between these two regions readily distinguishable, as illustrated by the white dashed line in Fig. 2 a). Of particular note, near the edge of the FZ, a significant refinement of the grain structure can be observed due to the influence of the cold HAZ on the solidification kinetics (refer to Fig. 2 b)). As one enters the FZ, the cold HAZ acts as a favorable substrate for grain nucleation. A dendritic solidification structures initiates at the interface between the HAZ and FZ, proceeding along the direction of the maximum temperature gradient perpendicular to the solid–liquid interface (i.e., towards the center of the weld). This competitive growth transitions into larger equiaxed grains (approximately ≈322 μm) as it approaches the vicinity of the weld centerline (refer to Fig. 2 b)). Based on the EBSD data near the HAZ/FZ interface shown in Fig. 2 a), the

inverse pole figure (IPF) map indicates that the grains in the FZ preferentially align with the (0 0 1) crystallographic orientation, which is in good agreement with the solidification theory of the face-centered cubic (FCC) structures.

Kernel Average Misorientation (KAM) analysis is used in crystallography to assess the internal orientation variations within grains. It characterizes the extent of orientation changes within a crystal by computing the average misorientation between a point within a grain and its neighbouring points. This parameter is commonly utilized to evaluate residual strains and plastic deformation within materials. Generally, a higher KAM value indicates a larger orientation difference (higher misorientation), which often correlates to a higher level of residual plastic strain. This relationship is governed by the localized increase in the density of Geometrically Necessary Dislocations (GND) [37,38]. Fig. 2 c) and d) depict the KAM and GND maps, respectively, for the CoCrFeMnNi welded joint with Monel 400 filler wire. To provide more clearly a depiction of the variations in KAM and GND values across the entire welded joint, Fig. 2c2) and d2) detail the changes in KAM and GND values along the central part of the joint's cross-section (refer to the yellow dashed lines in Fig. 2 c) and d)). When observing the color variations (refer to Fig. 2c1) and d1)), it becomes evident that there is a similarity in the color evolution between the KAM and GND maps. Both exhibit the deepest colors in the BM region, followed by the HAZ, and the lightest colors in the FZ, this translates into a higher KAM and GND values in BM and lower in the FZ. The spatial variation of KAM and GND values throughout the whole welded joint exhibits a concave shape (refer to Fig. 2 c 2) and d 2)). This pattern is indeed expected. In fact, the BM region has the highest KAM and GND values due to the extensive plastic deformation resulting from the rolling process imposed prior to welding. Upon entering the HAZ, the weld thermal cycle induces an annealing-like effect, releasing the pre-stored strain energy and consequently causing a natural decrease in the KAM and GND. The FZ, characterized by the least residual plastic strain, is a result of the rapid melting and solidification during welding, which eliminates the effects of previous thermomechanical processing on the properties. Here, it should be noted that while KAM/GND analysis quantifies overall internal orientation variations within grains, residual strains, and plastic deformation, it does not directly distinguish the specific contributions of each factor.

The color variations observed in the EDS mapping images (refer to Fig. 3) reveal that the main elements (Co, Cr, Fe, Mn, Ni and Cu, the latter one being only found in the FZ) are uniformly distributed without any evidence of macrosegregation. The uniform distribution of elements in the BM and HAZ is to be expected, since the weld thermal cycle cannot lead to a redistribution of elements within these two regions. However, it is worth noting that a change in color intensity can be observed, when transitioning from the HAZ to the FZ. This change is attributed to the complex elemental redistribution in the FZ, driven by the rapid solidification with intricate Marangoni flow, which is a characteristic feature of this region. Furthermore, the enrichment of Cu in the FZ originates from the mixing process between the Cu in the Monel 400 filler wire and the BM during welding. In this process, the combined effects of rapid solidification and Marangoni flow significantly contribute to the enrichment of Cu in the FZ. In contrast, other critical regions of the joint, such as the BM and the HAZ, exhibit a markedly different behaviour. Since these regions are not directly influenced by the Monel 400 filler wire and the forces of the weld heat cycles are insufficient to cause element redistribution within these regions, the enrichment phenomenon of Cu is not observed.

Fig. 4 a) and b) depict the superimposed high energy synchrotron X-ray diffraction plots covering the entire welded joint along with the corresponding contour plots. Combining these two plots (Fig. 4 a) and b)), it becomes evident that the diffracted intensities in the three distinct regions of the joint (BM, HAZ, and FZ) exhibit significant variations due to the influence of the weld thermal cycle which modifies the material texture. Specifically, the diffracted intensity gradually increases as one moves from the BM region into the HAZ. Upon entering the FZ, however, the intensity sharply decreases, reaching its lowest value. Based on the changes in diffraction intensity, the boundaries of these three typical regions can be clearly distinguished. Following this, considering the distance between neighboring diffraction lines (200 μm), the widths of the HAZ and FZ regions can be deduced to be ≈5.4 and ≈7.6 mm, respectively (half on each side of the joint), as illustrated in Fig. 4 b).

For deeper exploration into the impact of weld thermal cycles on the phase structure within the joint, Fig. 5 exhibits the phase identification results for the BM, HAZ and FZ obtained from synchrotron X-ray diffraction data. As expected, both the BM and HAZ show the presence of the typical FCC phase characteristic of CoCrFeMnNi HEA, while trace amounts of Cr-Mn oxide are also indexed (refer to Fig. 5 a) and b)). The formation of these oxides is related to material contamination as previously discussed in [28].

In the FZ, a more diverse phase structure is detected. Besides the matrix FCC phase and the Cr-Mn oxides, three distinct precipitated phases were identified: Cu-Ni-rich and Cu-Mn-rich FCC phases, as well as Cr-rich carbides. Oliveira et al. [32] performed gas tungsten arc welding on the present as-rolled CoCrFeMnNi HEA without the addition of filler wire, and observed that the FZ phase structure was solely composed of FCC and Cr-Mn oxides. Hence, it can be inferred that the emergence of these three precipitated phases (Cu-Ni-rich and Cu-Mn-rich FCC phases, as well as the Cr-rich carbides) can be predominantly

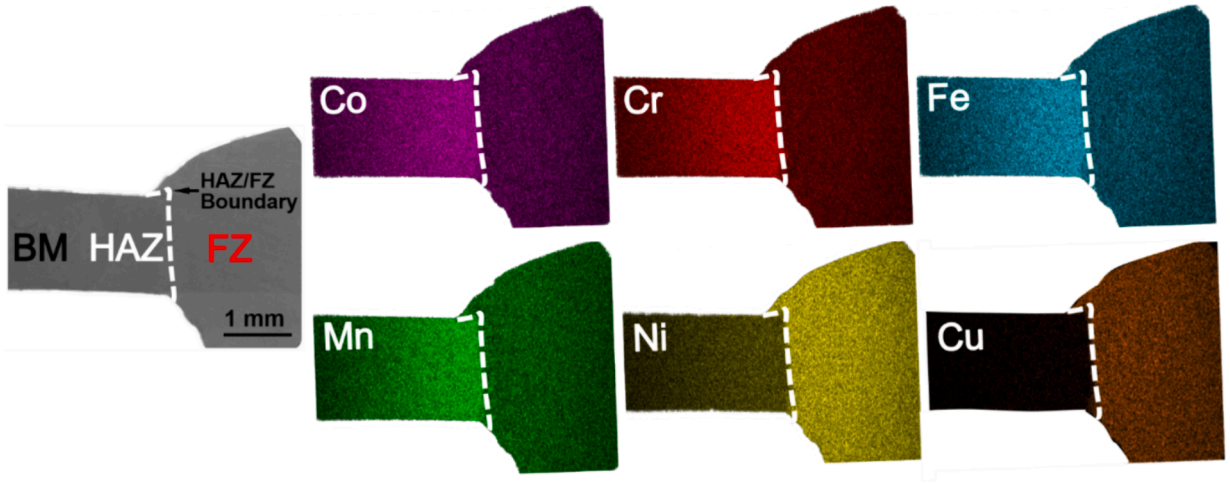

Fig. 3. EDS mapping of welded joint. Cu is only observed in the FZ since it comes from the Monel 400 filler material used for welding the CoCrFeMnNi HEA.

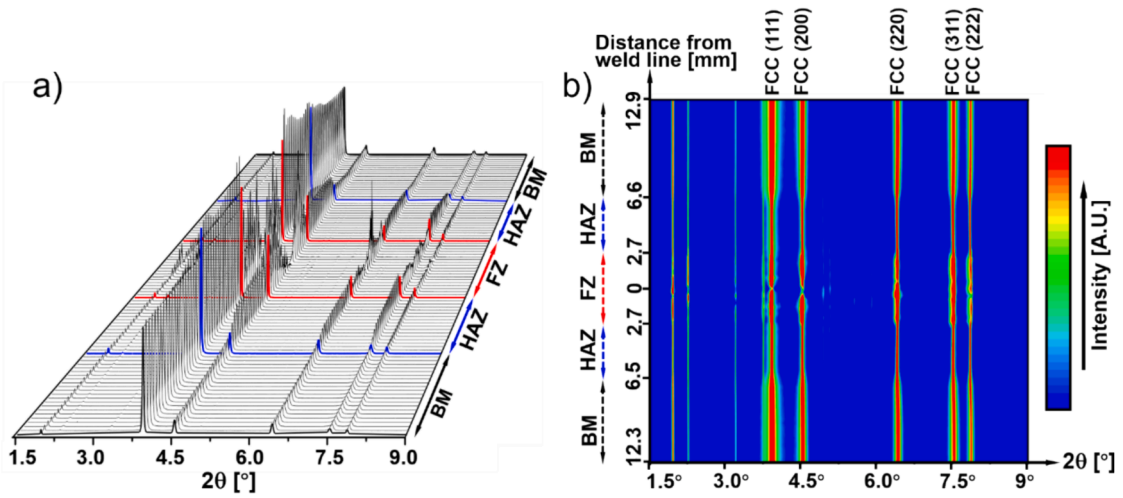

Fig. 4. a) Superimposed X-ray diffraction patterns across the welded joint; b) Intensity evolution of diffraction peaks after full-azimuthal angle integration.

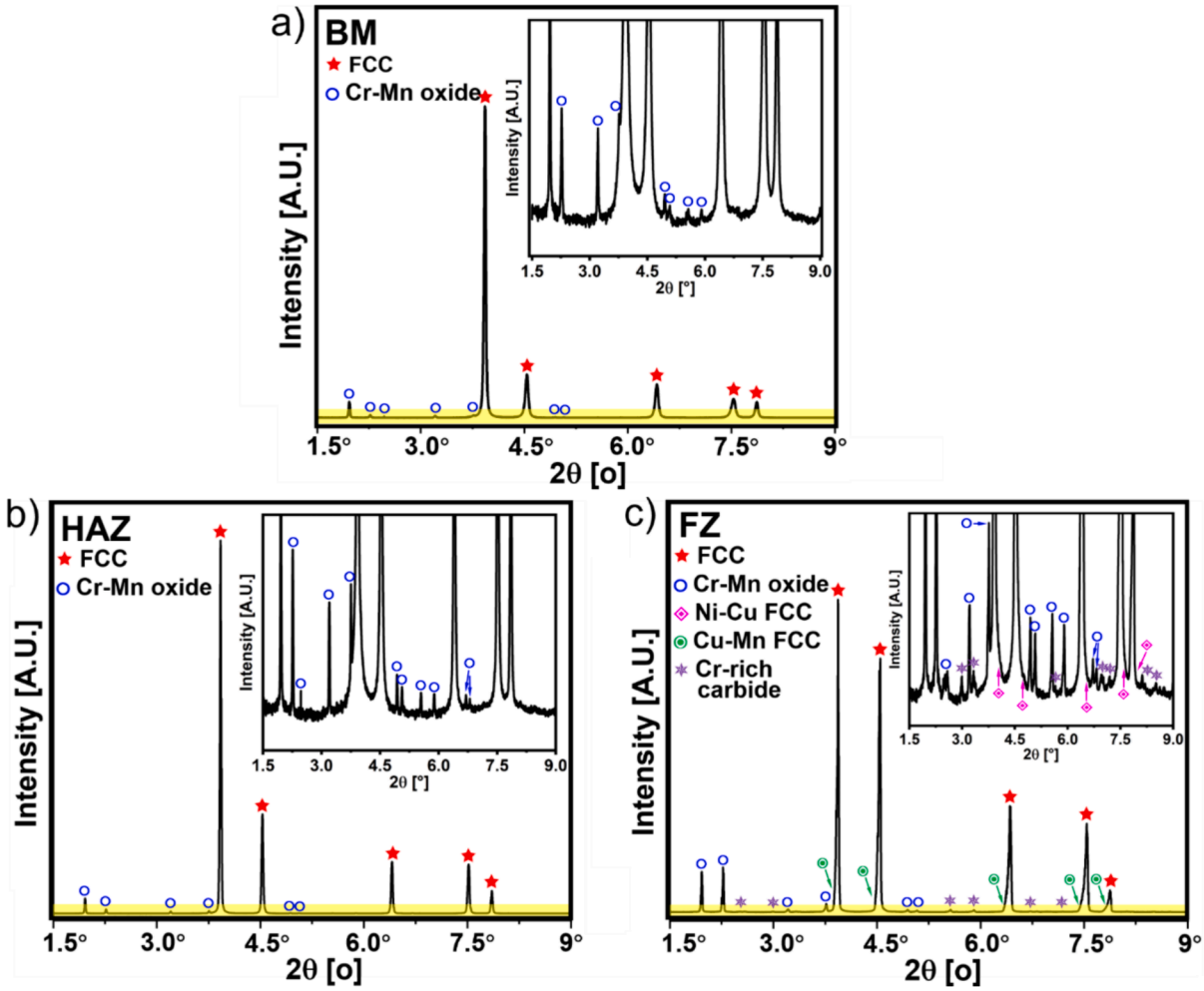

Fig. 5. Distinctive diffraction patterns were captured from: a) the BM; b) the HAZ; and c) the FZ. The yellow background highlights the magnified inserts for each panel. (For interpretation of the references to color in this figure legend, the reader is referred to the web version of this article.)

attributed to the introduction of the Monel 400 filler wire, which will drastically change the FZ chemistry and potentially the solidification path experienced by the material. Previous studies have demonstrated that the addition of Cu to CoCrFeMnNi HEAs can enhance phase separation and precipitation [39–41], with Cu playing a crucial role in determining the composition of nanoscale precipitates [42]. The sluggish diffusion effect within HEAs also contributes to the formation of Cu-rich nanoclusters [43,44], even for high cooling rate processes [43]. From a thermodynamic perspective, the diffusion of Ni in Cu is significantly faster than in other elements. Although Cu and Ni are typically

immiscible with each other, they can overcome their miscibility gap, when temperatures exceed 500 °C, displaying favorable solubility. Furthermore, Cu-Ni is a well-known isomorphous system [45], with similar atomic radii and electronegativity [46]. Consequently, Cu tends to nucleate with Ni [42]. Importantly, despite the higher Fe and Ni content in the FZ, their high compatibility prevents the formation of brittle intermetallic compounds [47]. As for the Cu-Mn-rich precipitated phase, it also showcases an FCC structure [48–50]. Earlier investigations [51] had substituted Ni for Cu in the CoCrFeMnNi HEA, revealing a strong repulsive interaction between Cu and the three other elements, Co, Cr, and Fe, resulting in phase separation. However, Cu readily forms a solid solution with Mn in the FCC phase. The formation of this Cu-Mn-rich precipitated phase [52] is driven by the reduction of entropy contribution, due to the declining mutual solubility between them as temperature decreases. The analysis of the phase structure in the FZ implies a pronounced tendency for Cu clustering in the CoCrFeMnNi HEA. This phenomenon has been similarly reported in other HEAs [53]. Regarding the occurrence of Cr-rich carbides in the FZ, it can be attributed to the carbon content in the Monel NiCu-7 filler wire, where Cr readily reacts with C.

To further validate the precipitates detected using synchrotron X-ray diffraction in the FZ, Fig. 6 presents the EDS composition measurements of small particles found in this region. These measurements provide additional confirmation of the presence of Cr-Mn oxides, Cu-Mn-rich, and Cu-Ni-rich phases within the FZ. Specifically, the yellow elliptical markers in Fig. 6 a) highlight the presence of Cr-Mn oxides. This finding aligns with the earlier synchrotron X-ray diffraction results (refer to Fig. 5 c)), thereby confirming the existence of this oxide in the FZ. Fig. 6 b) showcases two distinct precipitates: Cu-Mn precipitates and fine Ni-Cu precipitates with elongated needle-like shapes. This further supports the phase identification data obtained from the synchrotron X-ray diffraction measurements (refer to Fig. 5 c)). It should be noted that the absence of detection of Cr-rich carbides by EDS can be attributed to two primary reasons. Firstly, Cr-rich carbides might exist in the sample in the form of extremely small particles with a highly heterogeneous distribution. This characteristic makes it challenging for EDS to reliably detect their presence. Secondly, the spatial resolution limitations of EDS prevent the instrument from accurately identifying and distinguishing these small-scale carbides. Here, it is important to note that regarding the identification of precipitates in various regions of the welded joint using EDS and high-energy synchrotron radiation, only qualitative analysis has been conducted. Quantitative analysis, such as determining the size and distribution of precipitates, will be addressed in future work by using transmission electron microscopy and atom probe tomography. This aims to provide further clarification on the formation mechanisms of these precipitates and their impact on the mechanical properties of the welded joint.

The evaluation of the intensity variation of different diffraction peaks with respect to the azimuthal angle enables to get insights into the texture variation along the welded joint. When a material exhibit pronounced texture, the intensity of diffraction peaks is strengthened at certain azimuthal angles. This azimuthal angle dependence arises from the (preferential) orientation distribution of grains in the material, mirroring the concept of preferred orientation. The higher the intensity, the more significant the developed texture and its potential impact on the material properties.

Fig. 7 a1), b1), and c1) respectively depict the analyzed intensity evolution of the FCC diffraction peaks over the full azimuthal angle range (0 – 360°) for the three regions (BM, HAZ, and FZ) within the welded joint. Examining the diffraction intensity variation in relation to the azimuthal angle, it is perceived that (different) preferred orientation of the grains exists. Beginning with the BM (refer to Fig. 7 a1)), it shows a relatively smooth and continuous intensity distribution, particularly for the (1 1 1) lattice plane. This is due to the fact that the BM has undergone cold rolling, yielding fine grains (approximately ≈2 μm) and a fairly uniform texture distribution. In the HAZ (refer to Fig. 7 b1), the weld thermal cycle prompts grains that underwent deformation to regrow and rearrange (as indicated in EBSD results, refer to Fig. 2 b)). This leads to a fragmented and discontinuous characteristic in the orientation distribution of grains, manifested by interruptions or gaps in the diffracted peak intensity. Compared to the BM, it can be deduced that the weld thermal cycle alters the original grain orientation of the BM. Upon entering the FZ (refer to Fig. 7 c1)), the high-intensity spots are concentrated at specific azimuthal angles, indicating a robust texture presence in this region. This texture is linked to the coarse grain structure and directional solidification conditions. These texture characteristics reflect the changes in grain orientation and the evolution of grain size during the welding process.

Furthermore, micro-deformation also plays a significant factor in affecting the azimuthal angle-dependent position (2θ) of the diffraction peaks. When a material is subjected to compressive stresses, the position of the diffraction peak shifts towards higher 2θ angles. Conversely, under tensile stresses, the diffraction peak's position moves to a lower 2θ angle. This phenomenon stems from stress-induced changes in the crystal's interplanar spacing, named d-spacing, consequently leading to alterations in 2θ. As supporting evidence, Fig. 2 a2), b2), and c2) illustrate the relationship between the diffraction position of the (3 1 1) peak and the azimuthal angle. By analyzing the diffraction peak position of the (3 1 1) lattice plane, it is evident that stresses are present in all analyzed regions (BM, HAZ, and FZ), although their magnitude varies. In Fig. 7, one quadrant (0-90°) is chosen for quantitative analysis, where an azimuthal angle of 90° corresponds to the direction along the weld, and 0° represents the direction perpendicular to the weld. The stresses in these two directions are denoted as longitudinal stress and transverse

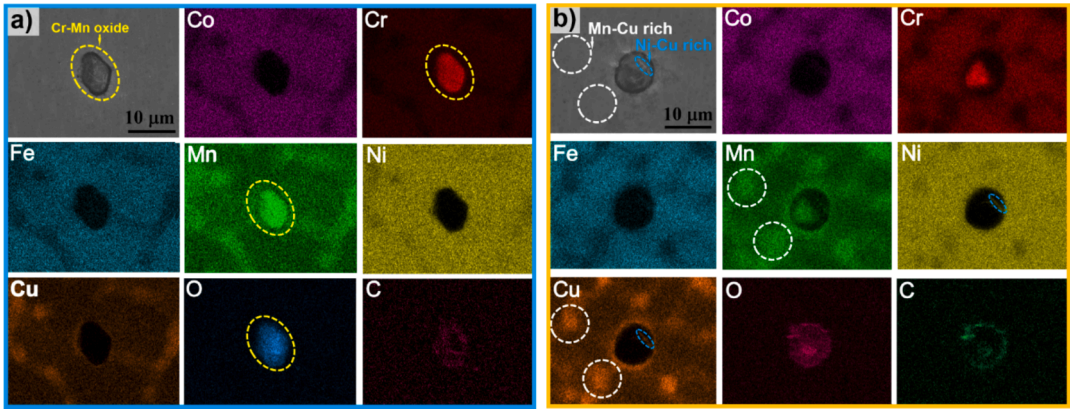

Fig. 6. SEM images along with their corresponding EDS mapping of different phase structures in the fusion zone: a) Cr-Mn oxide; b) Mn-Cu-rich and Ni-Cu rich FCC phases.

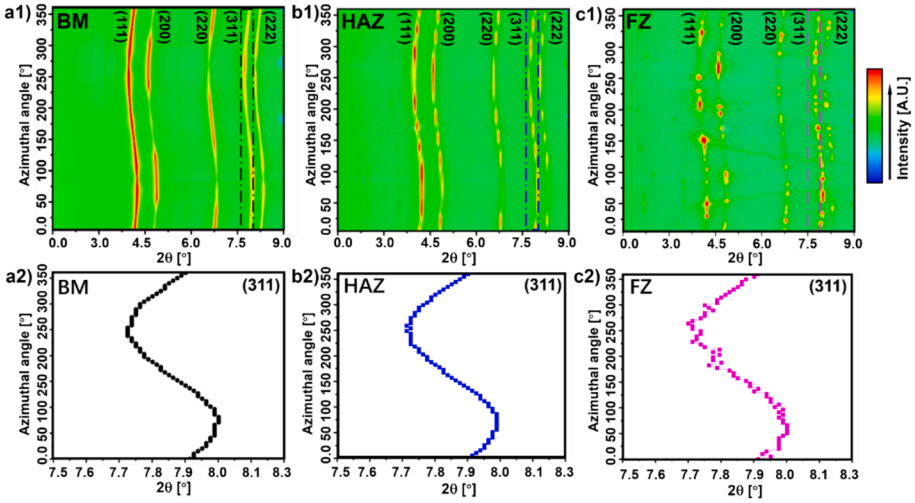

Fig. 7. Contour plot detailing the evolution of the diffracted peak intensities in representative regions of: a1) BM; b1) HAZ and c1) FZ. Diffraction peak intensity of FCC (3 1 1) diffraction peak as a function of azimuthal and diffraction angle in representative regions of: a2) BM; b2) HAZ and c2) FZ.

stress, respectively. The microstrain formula, given by $\varepsilon_{311} = (d_{311} - d_0) / d_0$, with d_0 representing the d-spacing value of the specimen in the stress-free condition, provides a method for calculating microstrain. However, since this study did not perform synchrotron analysis on a stress-free CoCrFeMnNi in the current work, thus a quantitative analysis of microstrain for the current welded joint is not conducted.

Moreover, the orientation distribution function (ODF) extracted from EBSD data was employed for quantitative texture analysis to further detail the impact of the weld thermal cycle on the material microstructure. The ODF is used to describe the distribution of crystal orientations. For materials with an FCC crystal structure, $\psi2 = 45°$, 65°, and 90° sections of the ODF are typically representative of the evolution of key texture components. Thus, this study selected these three sections for texture analysis. Table 3 summarizes the observed key texture components in the welded joint. In Fig. 8, a detailed comparison of the micro-texture evolution is presented for four regions (BM, low temperature HAZ, high temperature HAZ, and FZ) within the welded joint. Here, the low and high temperature HAZ are denominated as HAZ1 and HAZ2, respectively.

Overall, the weld thermal cycle effectively alters the texture components of the joint. Specifically, in the as-rolled CoCrFeMnNi BM, the crystal orientations primarily exhibit a γ-fiber texture (WD//<111>). The γ-fiber texture is reported to form near grain boundaries of deformed grains prior to annealing in the cold-rolling process [54], and represents a typical cold-rolled texture component [55] associated with excellent plastic deformation and mechanical properties. Additionally, a strong Cu texture component is observed, specifically along the (1 1 2) <111> direction, which is attributed to the inherently low stacking fault energy (SFE) of Co-Cr-Fe-Mn-Ni system HEAs [56]. In the HAZ (HAZ1 and HAZ2), where the thermal cycle imparted by the material resembles low- and high-temperature annealing treatments, respectively, the texture evolves due to the nucleation of new grains at grain boundaries via recrystallization, followed by grain growth, the latter being more predominant near the fusion boundary. This leads to a weakening of deformation texture components and an enhancement of the annealing texture components. In the HAZ1, the low-temperature annealing reduces the number of pre-existing grain boundaries, consequently weakening the γ-fiber texture. In this region, the main texture component is S (1 2 3) <634>, consistent with the texture observed in the $\psi2 = 65°$ section after annealing at 650 °C in a previous study on CoCrFeMnNi HEA [57]. In addition, the α-fiber (refer to the yellow dashed line) becomes more pronounced, representing a typical recrystallization texture, including the main texture components of (1 1 2) <110> and (2 2 3) <110> on the $\psi2 = 45°$ section. These findings align with those of Bhattacharjee et al., who investigated the texture evolution of recrystallized single-phase microstructures in cold-rolled HEAs [57]. Furthermore, in the HAZ2, the effect of a high-temperature annealing, favors an increase in the orientation density of cube texture (0 0 1) <100> increases in the $\psi2 = 90°$ section. This is associated to the formation of a large number of recrystallized grains, and has been reported multiple times in studies focusing on the thermomechanical processing of CoCrFeMnNi HEAs. In the FZ, a strong cube texture is observed, primarily attributed to the highly oriented grain growth in this region [58]. Also, the texture direction revealed in the FZ, (1 0 3) direction, is close to the easy-growth direction (0 0 1) of the FCC structure. The minor offset of 1.4° between the ideal growth direction and the observed one is attributed to the Marangoni flow, which can alter grain growth direction by changing the direction of heat flow [59].

Here, the correlation between texture evolution in the welded joint and mechanical properties may have multiple implications. Firstly, in the BM, the γ-fiber texture formed after cold rolling can enhance the material's strength and hardness in specific directions due to the specific orientation and arrangement of grains. However, this texture can also lead to reduced plasticity of the material in directions perpendicular to the fiber direction, as this specific arrangement of grains limits the deformability along that direction. Secondly, in the HAZ, the observed annealing texture can, on one hand, improve the material's ductility and impact toughness, as the newly formed grains typically have more uniform size and orientation, which helps reduce stress concentration effects and improve deformability. On the other hand, grain growth can decrease the material's tensile strength and hardness. Lastly, in the FZ, the strong cubic texture contributes to an improved isotropy of the material. The uniformity of grain orientation allows the material to deform more uniformly under stress, affecting its elastic behavior and making it easier to undergo deformation during manufacturing. In conclusion, texture changes induced during welding not only reflects changes in the material's microstructure but is also closely related to

Table 3
Main texture component information.

Texture component	Euler angles	Miller induces
E	(0°, 55°, 45°)	{1 1 1} <1 1 1>
Brass (Bs)	(35°, 45°, 90°)	{1 1 0} <1 1 2>
L	(90°, 45°, 90°)	{1 1 0} <1 1 1>
S	(59°, 37°, 63°)	{1 2 3} <6 3 4>
Copper (Cu)	(90°, 35°, 45°)	{1 1 2} <1 1 1>
Cube (C)	(0°, 0°, 0/ 90°)	{0 0 1} <1 0 0>
m-Brass	(50°, 65°, 63°)	29.6° <1 1 1>

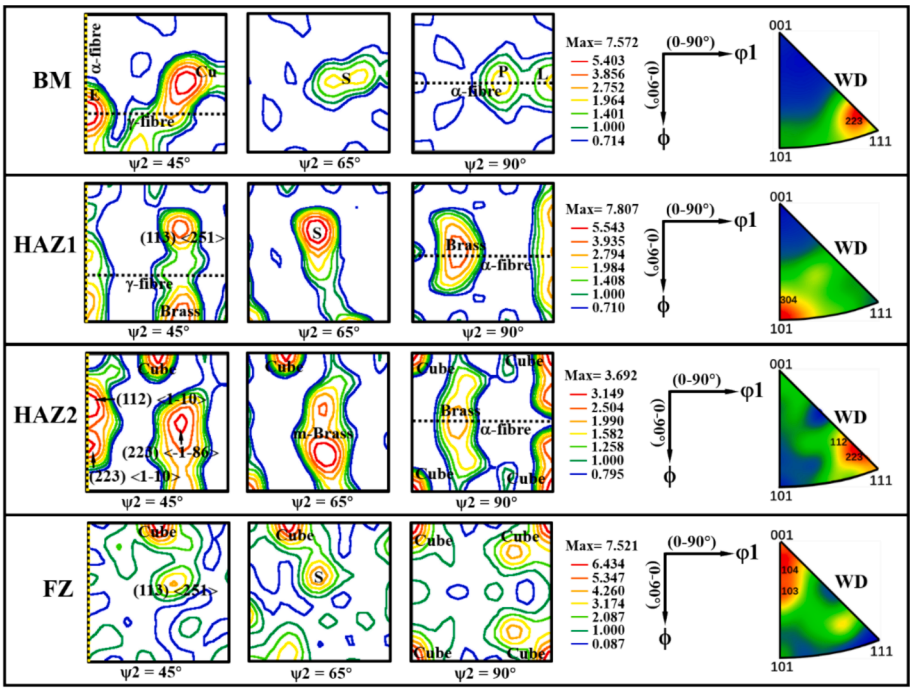

Fig. 8. Orientation distribution function (ODF) of four typical regions of the gas metal arc welded CoCrFeMnNi welded joint with Monel 400 filler wire: BM, HAZ1, HAZ2 and FZ.

resulting its (micro to macro) mechanical properties. Understanding these relationships is of significant importance for optimizing welding processes, improving material performance, and meeting specific performance requirements.

3.2. Thermodynamic calculations

To simulate the replication of the non-equilibrium solidification path and phase formation during the welding process, the Scheil-Gulliver model within ThermoCalc was utilized as a thermodynamic simulation tool. In this simulation work, the average composition obtained from EDS analysis of the FZ was utilized as the input elemental composition. Considering that carbon (C) can influence on phase formation and distribution during solidification, thus C was set as a fast diffuser. The simulation results are presented in Fig. 9. There it can be observed that during the non-equilibrium solidification process, the matrix FCC phase

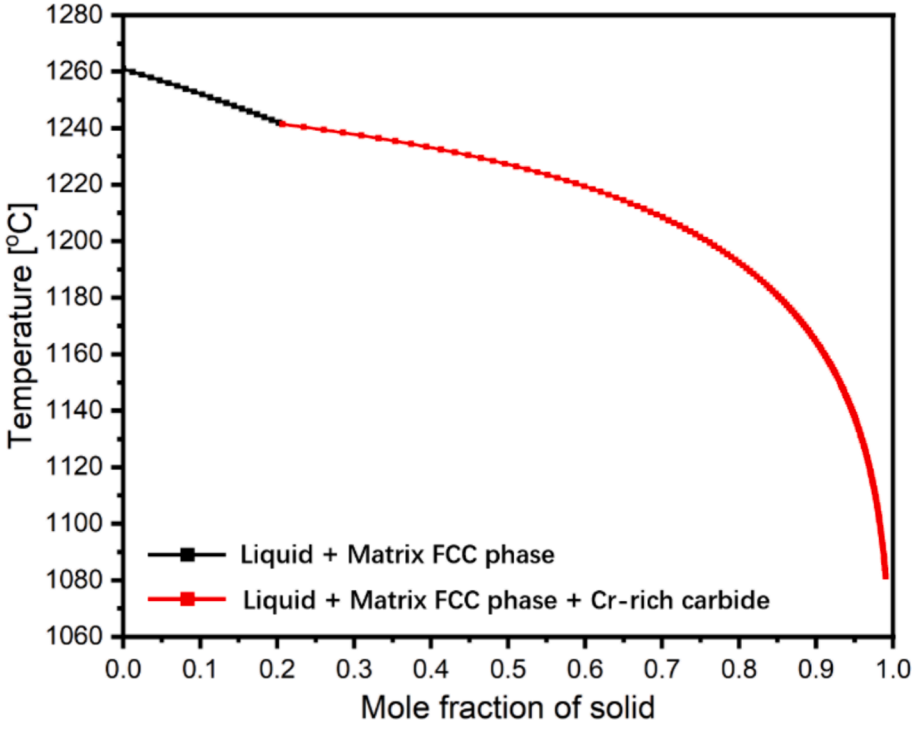

Fig. 9. Scheil-Gulliver calculations for the as-rolled CoCrFeMnNi high entropy alloy with Monel 400 filler wire welded joint.

forms initially. Then, this matrix FCC phase continues to form alongside with Cr-rich carbides. The solidification process is completed at approximately ≈1080 °C. Comparing with the phase identification results from the synchrotron X-ray diffraction data (refer to Fig. 5 c)), It is worth noting that the disparities between thermodynamic simulations and the actual presence of Cu-Ni and Cu-Mn FCC precipitate phases can be attributed to the following three primary factors: Firstly, thermodynamic models often face challenges in accurately predicting the behaviour of volatile elements in alloys, such as Mn, which can evaporate at elevated temperatures, resulting in deviations in chemical composition. Secondly, present models have limitations in predicting nucleation, and the kinetic behaviour of phase transformation and growth in multi-element alloys. Thirdly, differences between experimental conditions and model assumptions, such as assuming a uniform alloy composition or temperature distributions in the model, while actual experiments may involve non-uniform distribution of composition or temperature gradients. Although the thermodynamic calculations did not precisely predict the presence of Cu-Ni- and Cu-Mn-rich FCC phases, they successfully predict the existence of Cr-rich carbides. This addresses the limitation of EDS analysis (refer to Fig. 6) in detecting Cr-rich carbides. Furthermore, the presence of Cu-Ni- and Cu-Mn-rich phases detected through EDS analysis complements the lack of accuracy of thermodynamic simulations to predict these precipitates. The complementary use of both EDS analysis, synchrotron X-ray diffraction and thermodynamic simulations details that realistic thermodynamic predictions of the phase structure evolution during non-equilibrium solidification is yet incipient for multicomponent alloys, even if the present Co-Cr-Fe-Mn-Ni system is the most studied within the realm of HEAs.

Indeed, non-equilibrium solidification involves multiple factors, including rapid diffusion, elemental interactions and distribution. Moreover, the Marangoni effect renders that the composition within the fusion zone is not homogenous, the same following for the cooling conditions. Thus, the complex change in chemistry and solidification conditions within the welded joints can aid in the preferential formation of certain phases that are not thermodynamically predicted. Another possibility, as detailed above, is the yet incipient knowledge and database information for multicomponent alloys, which further increases the difficulty in accurately predicting the microstructure evolution during non-equilibrium solidification conditions as those typically found during fusion-based welding. Nonetheless, the present results can further aid in the development of more comprehensive databases for these materials towards an improved understanding of the physical metallurgy of this material system.

In the present case, the integration of the advantages of different advanced characterization techniques contributes to a deeper understanding of the solidification behavior. Corroboration between experimental results and thermodynamic simulations can deepen the understanding of the weld solidification behavior and the interpretation of phase structure evolution that arise during fast-cooling processes like fusion-based welding.

Elemental redistribution during the solidification process in the weld pool is a significant phenomenon in welding, exerting a considerable influence on the material weldability, susceptibility to hot cracking, microstructural characteristics of welds, and other performance aspects [60]. The partitioning coefficient (k) [61] stands as a pivotal parameter that provides insights into the possibility of alloying elements to distribute between liquid and solid phases during solidification. It also reflects the degree of micro-segregation between dendritic and interdendritic regions [62]. When the partitioning coefficient approaches 1, it indicates a uniform distribution of elements, which is an ideal behavior sought by material designers. In this case, the tendency for alloying elements to distribute between liquid and solid phases is minimal, resulting in a relatively uniform element distribution during the solidification process. However, when k exceeds 1, it suggests a preference for elements to partition into the solid phase during solidification, leading to the enrichment of specific elements in dendritic regions. Such segregation can potentially introduce instability in the joint performance, notably contributing to the occurrence of hot cracking and related issues, or (locally) altering the phase stability of the material. Conversely, when k is smaller than 1, it implies that certain elements are predominantly present in the liquid phase, which solidifies last, leading to their enrichment in interdendritic regions.

To determine the degree of elemental segregation during the solidification of the weld pool, partitioning coefficients of the main elements present in the FZ (Co, Cr, Fe, Mn, Ni, and Cu) were calculated using a dilution step of 10 %, as shown in Fig. 10. Here, a 0 % dilution corresponds to the FZ composed solely of the original BM (equiatomic CoCrFeMnNi), while 100 % dilution represents the FZ containing only the Monel 400 filler wire. The partitioning coefficients k can be observed as a function of dilution and temperature. Overall, across the entire dilution range, the partitioning coefficients for Mn and Cu are both less than 1, indicating a tendency for these elements to distribute to the interdendritic regions during solidification, thus resulting in Mn and Cu enrichment within these regions. Conversely, partitioning coefficients for Co, Cr, and Fe all exceed 1, implying a preference for these elements to partition into the dendritic regions. As for Ni, its partitioning coefficient approaches 1, suggesting a relatively uniform distribution between both dendritic and interdendritic regions.

The elemental composition of dendritic and interdendritic structures in the solidified microstructure of the FZ was further evaluated through EDS analysis (refer to Fig. 11). Evidently, the dendritic regions are composed of Fe, Co, Cr, and Ni, while the interdendritic regions are enriched with the lower melting point elements, Cu and Mn. The Ni element shows a relatively uniform distribution between these two regions. It is known that Co, Cr, Fe, and Ni contribute to the formation of FCC phase in the Co-Cr-Fe-Mn-Ni system, while the combination of Cu-Mn and Cu-Ni aids in the formation of precipitate phases [51]. Hence, it can be inferred that the previously detected Cu-Mn-rich and Cu-Ni-rich FCC precipitate phases in the FZ (refer to Fig. 5) are primarily concentrated in the interdendritic regions. It is noteworthy that the EDS area scan measurements align with the elemental redistribution behavior predicted by thermodynamic calculations (refer to Fig. 10). This implies that the calculated partitioning coefficients k can forecast and explain the phenomena of elemental redistribution and segregation during such non-equilibrium solidification process. This consistency further validates the reliability and accuracy of the research methodology and its results.

3.3. Mechanical properties

To further assess the influence of the weld thermal cycle on the strength across the joint, Fig. 12 a) presents the hardness mapping across it, while Fig. 12 b) shows the hardness distribution along the centerline of the weld, indicated by a black dashed line in Fig. 12 a), revealing the trend of hardness evolution throughout.

From a broader perspective (refer to Fig. 12 a)), the microhardness map distinctly differentiates the various regions within the welded joint: the blue region represents the BM, the transition from blue to yellow corresponds to the HAZ, and the red region stands for the FZ. Upon closer observation of the trend in hardness across the welded joint (refer to Fig. 12 b)), an overall U-shaped pattern becomes evident. Specifically, the hardness of the BM is the highest, at approximately ≈400 HV0.5. This highest hardness is attributed to the substantial plastic deformation that the BM underwent during the cold rolling process, leading to a significant accumulation of strain energy within the material. This phenomenon has been consistently verified in previous studies. As the material enters the HAZ, a softening behavior is evident as the hardness drops from around ≈400 HV0.5 in the BM to approximately ≈156 HV0.5 in the HAZ near the FZ. This softening is the combined result of strain energy release, and the effects of solid-state phase transformations (recovery, recrystallization, and grain growth). Specifically, the weld

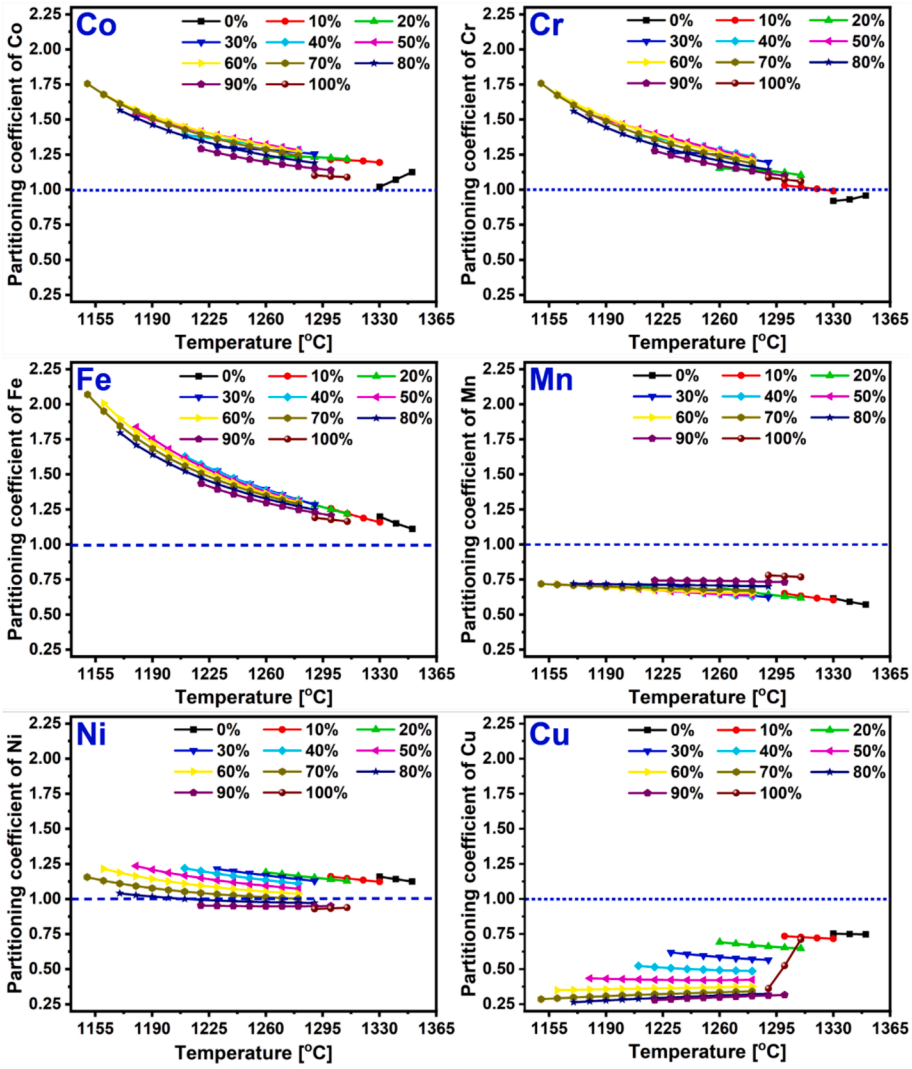

Fig. 10. Partitioning coefficients under various dilution conditions for Co, Cr, Fe, Mn, Ni, and Cu. At 0% dilution, the composition mirrors the equiatomic CoCrFeMnNi high entropy alloy (HEA), whereas 100% dilution corresponds to the Monel 400 alloy.

thermal cycles induce an annealing-like effect in this region, releasing the pre-stored strain energy/dislocations from the BM, and leading to its softening. Furthermore, the weld thermal cycle triggers recovery, recrystallization, and grain growth in this zone, with the influence on each of these solid-state transformations varying based on the distance from the weld centerline. According to the Hall-Petch effect, these recrystallized and subsequently grown grains typically lead to a reduction in hardness. Interestingly, upon entering the FZ, the hardness distribution does not follow the expected minimum value due to the presence of larger-sized grains (refer to Fig. 2 b)). Instead, the hardness in the FZ is slightly higher than the minimum hardness value in the HAZ (≈176 HV0.5 (FZ) vs. ≈156 HV0.5 (HAZ)). In comparison to prior studies [26,28,32] involving CoCrFeMnNi welded joints without any additional filer wire, and with the addition of the 400 and 308 stainless steels, the presence of Monel 400 filler material to the welded joints resulted in a notably higher hardness in the FZ (176 (current work) vs. 150 (CoCrFeMnNi without any filler wire) vs. 121 (CoCrFeMnNi with 400 stainless steel) vs. 142 (CoCrFeMnNi with 308 stainless steel)), this suggests that solid solution strengthening was achieved through the mixing of the CoCrFeMnNi HEA and Monel 400 filler wire, which enhanced the hardness in this region, compared to an as-cast or filler-free joint. Besides, in the FZ, slight fluctuations in microhardness are observed, which is related to the complex compositional and material flow changes induced by the typical chaotic liquid flow during fusion-based welding processes. It is worth noting that although residual stresses are potentially important factors influencing hardness distribution, in this study, based on the KAM and GND values obtained using EBSD technology for the entire joint (refer to Fig. 2 c1 and d1)), it is observed that residual plastic deformation in the HAZ and FZ was relatively small. Therefore, residual stresses were not considered as the primary influencing factor when exploring the patterns of hardness distribution. However, this does not mean that their influence can be completely disregarded. In fact, residual stresses, along with microstructural changes including grain size, phase structure, and distribution of precipitates, are all crucial factors affecting hardness distribution.

To explore the mechanical behavior of the gas metal arc welding in CoCrFeMnNi weld joint using Monel 400 filler wire, Fig. 13 a) presents the tensile stress–strain curve of the welded joint and BM counterpart. From this, it is evident that the as-rolled BM showcases an ultimate strength of approximately ≈948 MPa and an elongation of about ≈9.5 %. In contrast, the gas metal arc (GMA) welded joint retains approximately ≈72 % of the tensile strength of BM (≈687 MPa) and about ≈83 % of its elongation (≈7.9 % vs. ≈9.5 %). The difference in mechanical properties between the BM and the welded joint arises from various factors, including microstructural evolution in the HAZ, FZ, existing of a weld toe originated from the welding process, as well as potential

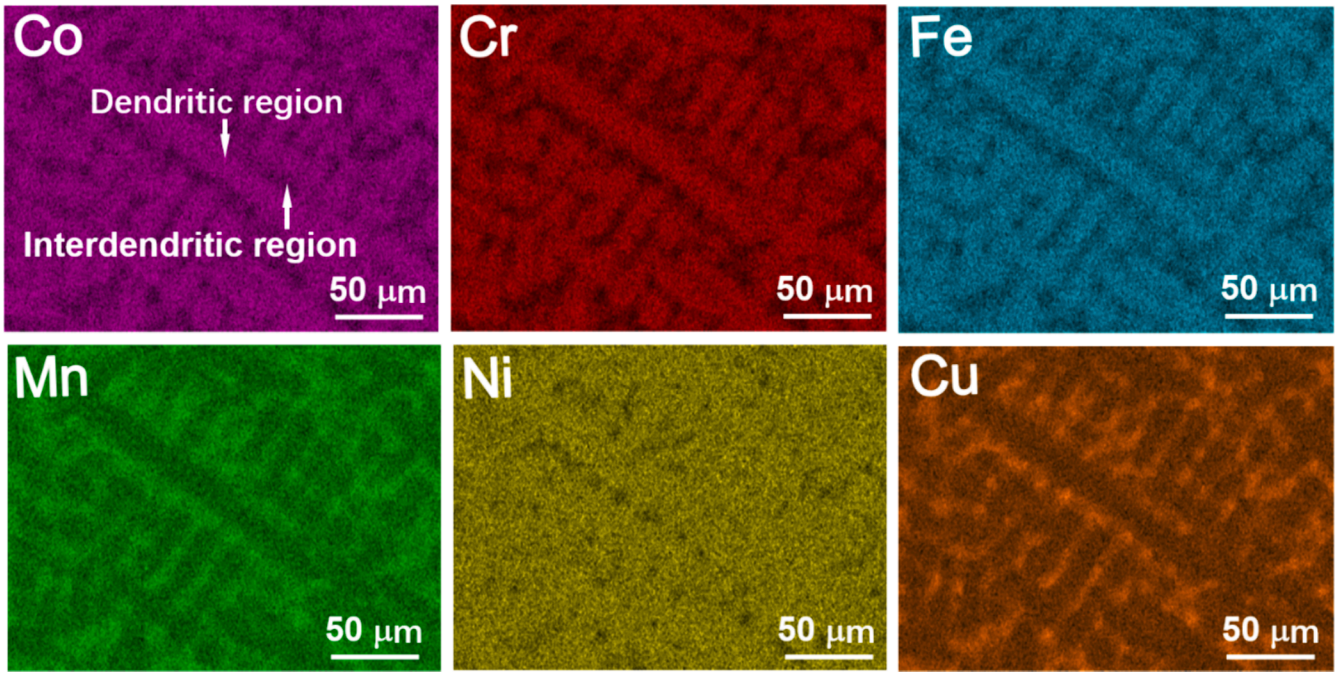

Fig. 11. EDS maps in the FZ.

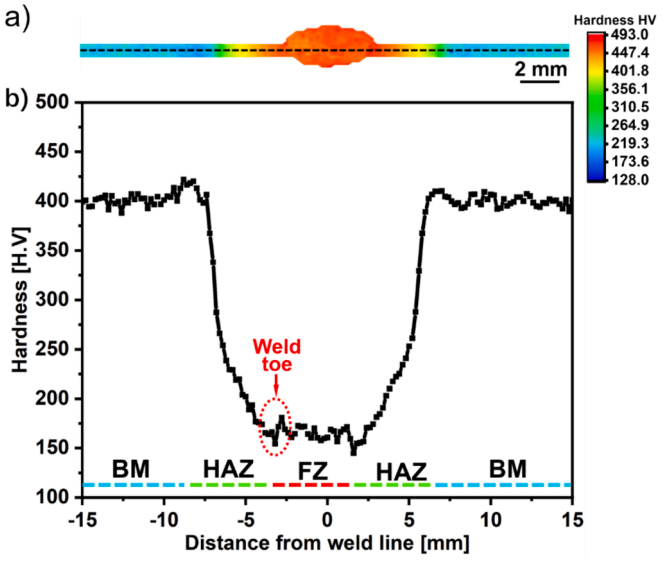

Fig. 12. a) Microhardness distribution mapping throughout the whole welded joint; b) Microhardness profiles extracted along the central axis of the joint (highlighted by the black dashed line in Fig. 12a).

residual stresses. It should be noted that this difference is the result of the interaction and combined effect of the various factors mentioned above, rather than the result of the action of a single factor. Despite the reduction in both ultimate strength and elongation in the post-welded joint compared to the BM, such decrease in mechanical properties is still acceptable due to the medium to high strength/ductility combination.

For a comprehensive understanding of the mechanical behavior across various regions of the welded joint, Fig. 13 b) illustrates the stress–strain curves obtained through DIC for four distinct regions: BM, HAZ, weld toe, and FZ. Additionally, DIC contour maps are presented to visualize the strain distribution across the joint. From the Fig. 13 b), it is evident that different regions of the welded joint exhibit distinct mechanical behaviors during tensile deformation. When comparing the stress–strain curves of these regions (refer to Fig. 13 b)), the BM shows the least deformation, followed by the FZ, then the HAZ, with the largest deformation being observed at the weld toe (fracture site). The observed variation in deformation among these regions correlates closely with their respective strength characteristics, as inferred from the microhardness measurements. Under loading, deformation initiates in the relatively softer HAZ and FZ, particularly concentrated at the weld toe region, where the hardness is lowest (refer to Fig. 12 b)). Nevertheless, due to the FZ's cross-sectional area being nearly three times larger than that of the HAZ, the stress per unit area in the FZ is notably lower under the same applied load. Consequently, the experienced deformation in the FZ is smaller than that in the HAZ. The BM, having the highest hardness, naturally exhibits the least deformation during tension. By observing the DIC contour map near the point of fracture, the location of fracture initiation (refer to Fig. 13 b) at the weld toe becomes apparent. This also reveals the underlying factors contributing to the tensile fracture. Key factors include: the soft characteristic of the weld toe region (refer to Fig. 12 b)) prone to plastic deformation accumulation, the significant microstructural differences between the weld toe and the adjacent FZ, particularly evident in pronounced grain size gradients, as well as the existence of geometric defects at the weld toe leading to stress concentration effects.

In conclusion, the findings from Fig. 13 a) and b) offer vital insights for a comprehensive understanding of the mechanical performance, deformation distribution, and fracture mechanisms of the welded joint. These research outcomes hold significant implications for guiding future endeavors towards optimizing welding processes and selecting appropriate materials and contribute to bolstering the reliability and performance of welded joints in real-world applications. Future work will envisage the improvement of the mechanical properties of these CrMnFeCoNi welded joints using post-weld heat treatments as successfully performed by outro groups [63,64].

Fig. 14 provides a detailed representation of the fractured surface of the welded joint. In Fig. 14 a), the overall macroscopic morphology of the entire welded joint fracture is illustrated. The presence of numerous and uniformly distributed dimples serves as confirmation of evidence indicating a ductile fracture in the welded joint. The existence of these dimples aligns with the high ductility demonstrated by the joint under

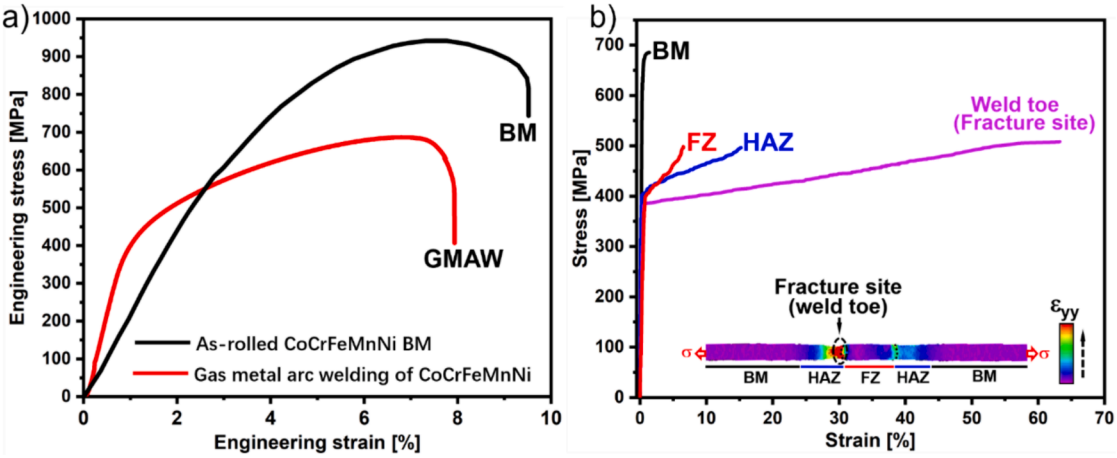

Fig. 13. a) Mechanical behavior of the as-rolled CoCrFeMnNi BM and as-welded HEA joints obtained from tensile testing until failure; b) Tensile curves obtained from digital image correlation measurements for different regions across the joint: BM, HAZ, weld toe and FZ (the insert strain maps obtained from DIC).

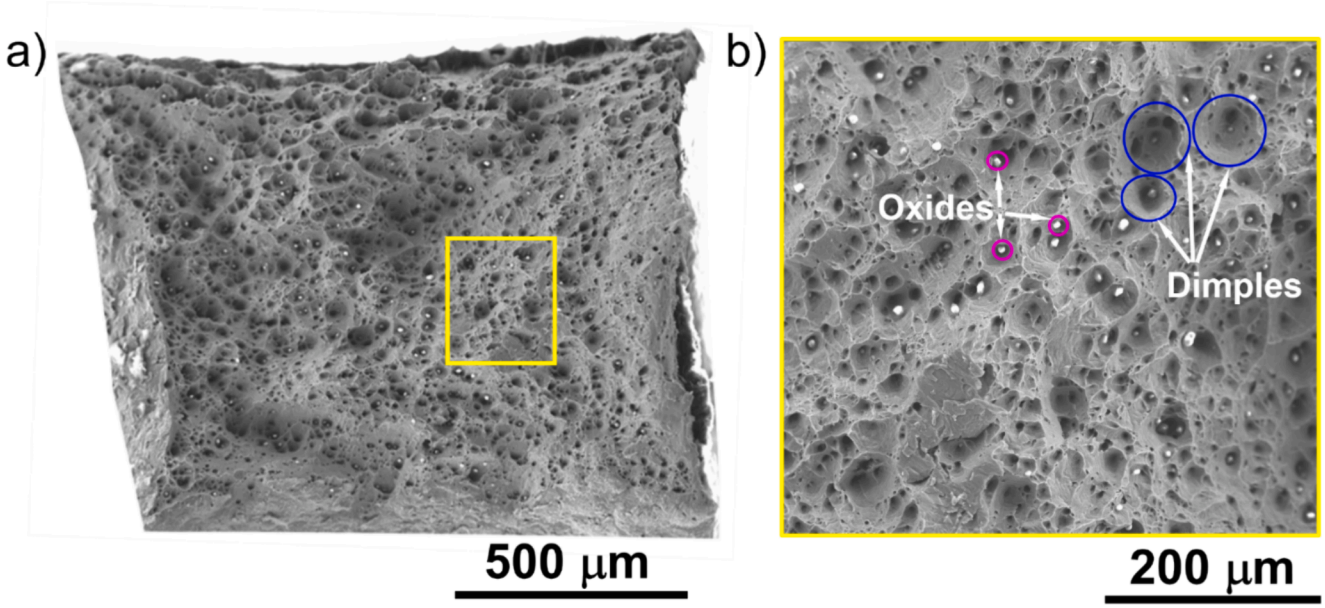

Fig. 14. Fractography of the welded joint: a) overview of a fractured sample; b) close-up highlighting a ductile-like morphology and dimples of the fracture surface.

study, as inferred from the DIC analysis. In Fig. 14 b), the presence of small particles is noted, and previous research has substantiated that these particles are oxides. Although these oxide precipitates are found at the fracture surface, they do not contribute to a mechanism of brittle fracture in these welded joints. This suggests that, despite the presence of such oxides, they are not the primary cause of brittle fracture in the welded joint. This, once again, reinforces prior analytical conclusions regarding potential causes of joint fracture, encompassing plastic accumulation in the weld toe region, microstructural differences between the weld toe and adjacent FZ, and stress concentration arising from geometric defects at the weld toe.

To comprehensively summarize the microstructural evolution and mechanical properties across various regions (BM, HAZ near the BM, HAZ near the FZ, and FZ) investigated in this study, Table 4 offers a comprehensive overview of observed changes. It compiles essential microstructural characteristics and mechanical properties for each region, encompassing grain size, phase composition, texture evolution, hardness variation, and mechanical performance across the different regions.

Table 4
Summary of the evolution of grain size, phase structure, texture, hardness and mechanical properties in different regions of the welded joint.

	BM	HAZ near BM	HAZ near FZ	FZ
Grain size	≈2 µm	≈23.2 µm	≈49.86 µm	≈322 µm
Phase structure	FCC; Cr-Mn oxide	FCC; Cr-Mn oxide	FCC; Cr-Mn oxide	FCC; Cr-Mn oxide; Ni-Cu FCC; Cu-Mn FCC; Cr-rich carbide
Texture	γ-fibre	S (123) ⟨634⟩	Cube	Cube
Hardness	≈400	From ≈400 decreases to ≈156	≈176	
Mechanical properties	ε ≈1.46 %; σ ≈691.26 MPa	ε ≈15.24 %; σ ≈96 MPa	ε ≈6.47 %; σ ≈501.84 MPa	

4. Conclusions

This study conducted an in-depth investigation into the weldability of CoCrFeMnNi HEA using gas metal arc welding (GMAW) with Monel 400 filler wire. The key findings drawn from the present research are as follows:

1) A reliable metallurgical compatibility was observed between the as-rolled CoCrFeMnNi HEA and Monel 400 alloy.
2) The weld thermal cycle induced changes in both the microstructure, both grain structure, phases and texture components of the welded joint. Solid-state transformations in the HAZ led to softening of this region.
3) The introduction of Monel 400 wire in the FZ induced solid solution strengthening effects.
4) High-energy synchrotron X-ray diffraction allowed to determine the phase structures in the welded joint. Mismatch between experimentally observed and thermodynamic predicted phases are discussed based on the yet incipient thermodynamic information for multicomponent alloys and complex mixing and element composition within the FZ.
5) Although CoCrFeMnNi welded joints with 400 filler wires have ≈72 % (≈687 vs. ≈948 MPa) and ≈83 % (≈7.9 % vs. ≈9.5 %) of the ultimate strength and elongation of the BM, respectively, this reduction in mechanical properties is still acceptance due to the good balance of strength/ductility of the welded joint.

In conclusion, this study not only serves as a crucial reference for optimizing welding processes in manufacturing industries such as aerospace, automotive, and shipbuilding, but also lays a solid theoretical foundation for developing advanced welding techniques tailored to specific material compositions and application requirements. Looking forward, further research can explore various filler materials and welding techniques to better understanding their impact on the mechanical properties and microstructure of welded joints under diverse conditions, thereby offering more precise guidance for practical applications. Additionally, investigating the long-term stability and durability of welded structures in real-world operating environments will deepen understanding of their reliability and service life, facilitating more robust structural design practices.

CRediT authorship contribution statement

Jiajia Shen: Writing – review & editing, Writing – original draft, Visualization, Validation, Software, Methodology, Investigation, Formal analysis, Data curation, Conceptualization. **Yeon Taek Choi:** Investigation, Data curation. **Rita Gonçalves:** Investigation. **Norbert Schell:** Investigation. **Jin Yang:** Investigation. **Zhi Zeng:** Investigation. **Ana Catarina Baptista:** Investigation. **Hyoung Seop Kim:** Investigation, Writing – review & editing. **J.P. Oliveira:** Writing – review & editing, Writing – original draft, Visualization, Validation, Supervision, Resources, Project administration, Methodology, Investigation, Funding acquisition, Formal analysis, Conceptualization.

Declaration of competing interest

The authors declare that they have no known competing financial interests or personal relationships that could have appeared to influence the work reported in this paper.

Data availability

Data will be made available on request.

Acknowledgments

JS and JPO acknowledge Fundação para a Ciência e a Tecnologia (FCT - MCTES) for its financial support via the project UID/00667/2020 (UNIDEMI). JPO acknowledges the funding of CENIMAT/i3N by national funds through the FCT-Fundação para a Ciência e a Tecnologia, I. P., within the scope of Multiannual Financing of R&D Units, reference UIDB/50025/2020-2023. JS acknowledges the China Scholarship Council for funding the Ph.D. grant (CSC NO. 201808320394). This work was supported by the National Research Foundation of Korea (NRF) with a grant funded by the Korea government (MSIP) (NRF-2021R1A2C3006662). The authors acknowledge DESY (Hamburg, Germany), a member of the Helmholtz Association HGF, for the provision of experimental facilities. Beamtime was allocated for proposal I-20210899 EC. The research leading to this result has been supported by the project CALIPSOplus under the Grant Agreement 730872 from the EU Framework Programme for Research and Innovation HORIZON 2020.

References

[1] D.B. Miracle, O.N. Senkov, A critical review of high entropy alloys and related concepts, Acta Mater. 122 (2017) 448–511, https://doi.org/10.1016/j.actamat.2016.08.081.
[2] W. Li, D. Xie, D. Li, Y. Zhang, Y. Gao, P.K. Liaw, Mechanical behavior of high-entropy alloys, Prog. Mater. Sci. 118 (2021) 100777, https://doi.org/10.1016/j.pmatsci.2021.100777.
[3] Y. Wang, G. Li, H. Li, Y. Mu, K. Sun, W. Zhao, Y. Da Li, G.W. Jia, Effect of aging on corrosion resistance of (FeCoNi)86Al7Ti7 high entropy alloys, Corros. Sci. 227 (2024) 111717, https://doi.org/10.1016/j.corsci.2023.111717.
[4] Y. Gao, K. Chong, C. Liu, Y. Cao, D. Wu, Y. Zou, Electrochemical corrosion and high temperature hot corrosion behavior of NbTaTiV and CrNbTaTiV high entropy alloy, J. Mater. Res. Technol. 28 (2024) 216–234, https://doi.org/10.1016/j.jmrt.2023.11.247.
[5] K. Wang, Y. Zhu, P. Wang, X. Li, B. Malomo, L. Yang, Enhancing corrosion resistance in CoCrFeNiTa high entropy alloys via Mo addition, Electrochim. Acta. 480 (2024) 143951, https://doi.org/10.1016/j.electacta.2024.143951.
[6] M. Li, H. Henein, C. Zhou, J. Liu, Towards high-entropy alloys with high-temperature corrosion resistance and structural stability, J. Mater. Sci. Technol. 174 (2024) 133–144, https://doi.org/10.1016/j.jmst.2023.07.035.
[7] Y. Yuan, J.J. Wang, J. Wei, W.Y. Chen, H.L. Yan, N. Jia, Cu alloying enables superior strength-ductility combination and high corrosion resistance of FeMnCoCr high entropy alloy, J. Alloys Compd. 970 (2024) 172543, https://doi.org/10.1016/j.jallcom.2023.172543.
[8] X. Gao, W. Jiang, Y. Lu, Z. Ding, J. Liu, W. Liu, G. Sha, T. Wang, T. Li, I.T.H. Chang, Y. Zhao, Excellent strength-ductility combination of Cr26Mn20Fe20Co20Ni14 high-entropy alloy at cryogenic temperatures, J. Mater. Sci. Technol. 154 (2023) 166–177, https://doi.org/10.1016/j.jmst.2023.01.023.
[9] T. Li, S. Wang, W. Fan, Y. Lu, T. Wang, T. Li, P.K. Liaw, CALPHAD-aided design for superior thermal stability and mechanical behavior in a TiZrHfNb refractory high-entropy alloy, Acta Mater. 246 (2023) 118728, https://doi.org/10.1016/j.actamat.2023.118728.
[10] K. Lu, A. Chauhan, D. Litvinov, A.S. Tirunilai, J. Freudenberger, A. Kauffmann, M. Heilmaier, J. Aktaa, Micro-mechanical deformation behavior of CoCrFeMnNi high-entropy alloy, J. Mater. Sci. Technol. 100 (2022) 237–245, https://doi.org/10.1016/j.jmst.2021.04.079.
[11] P. Ramakrishnan, Welding metallurgy, Indian Weld. J. 4 (1972) 89, https://doi.org/10.22486/iwj.v4i3.150243.
[12] J. Li, K. Yamanaka, Y. Zhang, T. Furuhara, G. Cao, J. Hu, A. Chiba, Reaching unconventionally large Hall-Petch coefficients in face-centered cubic high-entropy alloys, Mater. Res. Lett. 12 (2024) 399–407, https://doi.org/10.1080/21663831.2024.2337211.
[13] J.G. Lopes, J.P. Oliveira, A short review on welding and joining of high entropy alloys, Metals (basel). 10 (2020) 212, https://doi.org/10.3390/met10020212.
[14] T. Sonar, M. Ivanov, E. Trofimov, A. Tingaev, I. Suleymanova, A critical review on solid-state welding of high entropy alloys– processing, microstructural characteristics and mechanical properties of joints, Def. Technol. (2023), https://doi.org/10.1016/j.dt.2023.08.001.
[15] S. Li, X. Hou, X. Wang, Z. Liu, Y. Xia, H. Dong, Weldability of high entropy alloys: Microstructure, mechanical property, and corrosion resistance, J. Manuf. Process. 99 (2023) 209–229, https://doi.org/10.1016/j.jmapro.2023.05.049.
[16] Z. Wu, S.A. David, Z. Feng, H. Bei, Weldability of a high entropy CrMnFeCoNi alloy, Scr. Mater. 124 (2016) 81–85, https://doi.org/10.1016/j.scriptamat.2016.06.046.
[17] M.-G. Jo, H.-J. Kim, M. Kang, P.P. Madakashira, E.S. Park, J.-Y. Suh, D.-I. Kim, S.-T. Hong, H.N. Han, Microstructure and mechanical properties of friction stir welded and laser welded high entropy alloy CrMnFeCoNi, Met. Mater. Int. 24 (2018) 73–83, https://doi.org/10.1007/s12540-017-7248-x.

[18] H. Nam, C. Park, C. Kim, H. Kim, N. Kang, Effect of post weld heat treatment on weldability of high entropy alloy welds, Sci. Technol. Weld. Join. 23 (2018) 420–427, https://doi.org/10.1080/13621718.2017.1405564.
[19] N. Kashaev, V. Ventzke, N. Stepanov, D. Shaysultanov, V. Sanin, S. Zherebtsov, Laser beam welding of a CoCrFeNiMn-type high entropy alloy produced by self-propagating high-temperature synthesis, Intermetallics. 96 (2018) 63–71, https://doi.org/10.1016/j.intermet.2018.02.014.
[20] Y. Hu, Y. Niu, Y. Zhao, W. Yang, X. Ma, J. Li, Friction stir welding of CoCrNi medium-entropy alloy: Recrystallization behaviour and strengthening mechanism, Mater. Sci. Eng. A. 848 (2022) 143361, https://doi.org/10.1016/j.msea.2022.143361.
[21] Y. Lu, X. Zhang, H. Wang, C. Kan, F. Zhang, P. Dai, H. Wang, Investigation of microstructure, texture, and mechanical properties of FeCoNiCrMn high entropy alloy during drive friction welding, Mater. Charact. 189 (2022) 111959, https://doi.org/10.1016/j.matchar.2022.111959.
[22] J.-Y. Lin, Z.-H. Lai, T. Otsuki, H.-W. Yen, S. Nambu, Gradient microstructure and interfacial strength of CoCrFeMnNi high-entropy alloy in solid-state ultrasonic welding, Mater. Sci. Eng. A. 825 (2021) 141885, https://doi.org/10.1016/j.msea.2021.141885.
[23] S.S. Nene, K. Liu, M. Frank, R.S. Mishra, R.E. Brennan, K.C. Cho, Z. Li, D. Raabe, Enhanced strength and ductility in a friction stir processing engineered dual phase high entropy alloy, Sci. Rep. 7 (2017) 16167, https://doi.org/10.1038/s41598-017-16509-9.
[24] H. Nam, B. Moon, S. Park, N. Kim, S. Song, N. Park, Y. Na, N. Kang, Gas tungsten arc weldability of stainless steel 304 using CoCrFeMnNi filler metals for cryogenic applications, Sci. Technol. Weld. Join. 27 (2022) 33–42, https://doi.org/10.1080/13621718.2021.1996851.
[25] P. Zhang, Y. Qi, Q. Cheng, X. Sun, Welding dissimilar alloys of CoCrFeMnNi high-entropy alloy and 304 stainless steel using gas tungsten arc welding, J. Mater. Eng. Perform. (2023), https://doi.org/10.1007/s11665-023-08229-1.
[26] J. Shen, R. Gonçalves, Y.T. Choi, J.G. Lopes, J. Yang, N. Schell, H.S. Kim, J. P. Oliveira, Microstructure and mechanical properties of gas metal arc welded CoCrFeMnNi joints using a 308 stainless steel filler metal, Scr. Mater. 222 (2023) 115053, https://doi.org/10.1016/j.scriptamat.2022.115053.
[27] H. Nam, S. Park, N. Park, Y. Na, H. Kim, S.-J. Yoo, Y.-H. Moon, N. Kang, Weldability of cast CoCrFeMnNi high-entropy alloys using various filler metals for cryogenic applications, J. Alloys Compd. 819 (2020) 153278, https://doi.org/10.1016/j.jallcom.2019.153278.
[28] J. Shen, R. Gonçalves, Y.T. Choi, J.G. Lopes, J. Yang, N. Schell, H.S. Kim, J. P. Oliveira, Microstructure and mechanical properties of gas metal arc welded CoCrFeMnNi joints using a 410 stainless steel filler metal, Mater. Sci. Eng. A. 857 (2022) 144025, https://doi.org/10.1016/j.msea.2022.144025.
[29] A. Mukhopadhyay, D.K. Urkude, G. Mukhopadhyay, Effect of cold work on hydrogen embrittlement of monel-400, J. Fail. Anal. Prev. 24 (2024) 279–290, https://doi.org/10.1007/s11668-023-01836-z.
[30] C.J. Farnin, E.N. Coker, P.A. Salinas, J.N. DuPont, The influence of nominal composition on the microstructure, tensile properties, and weldability of cast monel alloys, Metall. Mater. Trans. A. 55 (2024) 580–597, https://doi.org/10.1007/s11661-023-07269-5.
[31] H. Dai, S. Shi, J. Tang, C. Guo, Z. Ning, X. Chen, Revealing the effect of heat treatment on stress corrosion cracking behavior of Monel 400 alloy in hydrofluoric acid vapor environment, Corros. Sci. 215 (2023) 111046, https://doi.org/10.1016/j.corsci.2023.111046.
[32] J.P. Oliveira, T.M. Curado, Z. Zeng, J.G. Lopes, E. Rossinyol, J.M. Park, N. Schell, F. M. Braz Fernandes, H.S. Kim, Gas tungsten arc welding of as-rolled CrMnFeCoNi high entropy alloy, Mater. Des. 189 (2020) 108505, https://doi.org/10.1016/j.matdes.2020.108505.
[33] J.P. Oliveira, T.G. Santos, R.M. Miranda, Revisiting fundamental welding concepts to improve additive manufacturing: From theory to practice, Prog. Mater. Sci. 107 (2020) 100590, https://doi.org/10.1016/j.pmatsci.2019.100590.
[34] M. Ma, R. Lai, J. Qin, B. Wang, H. Liu, D. Yi, Effect of weld reinforcement on tensile and fatigue properties of 5083 aluminum metal inert gas (MIG) welded joint: Experiments and numerical simulations, Int. J. Fatigue. 144 (2021) 106046, https://doi.org/10.1016/j.ijfatigue.2020.106046.
[35] J.G. Lopes, D. Martins, K. Zhang, B. Li, B. Wang, X. Wang, N. Schell, E. Ghafoori, A. C. Baptista, J.P. Oliveira, Unveiling the microstructure evolution and mechanical properties in a gas tungsten arc-welded Fe–Mn–Si–Cr–Ni shape memory alloy, J. Mater. Sci. (2024), https://doi.org/10.1007/s10853-024-09606-4.
[36] F. An, L. Zhang, J. Wu, M. Wang, M. Xie, Influences of solution temperature on microstructures and performance of electron beam welded joints of laser powder bed fusion TC11 thin-walled samples, Mater. Charact. (2024) 113926, https://doi.org/10.1016/j.matchar.2024.113926.
[37] Y. Liu, J. Ren, S. Guan, C. Li, Y. Zhang, S. Muskeri, Z. Liu, D. Yu, Y. Chen, K. An, Y. Cao, W. Liu, Y. Zhu, W. Chen, S. Mukherjee, T. Zhu, W. Chen, Microstructure and mechanical behavior of additively manufactured CoCrFeMnNi high-entropy alloys: Laser directed energy deposition versus powder bed fusion, Acta Mater. 250 (2023) 118884, https://doi.org/10.1016/j.actamat.2023.118884.
[38] Y. Liu, Y. Cao, Q. Mao, H. Zhou, Y. Zhao, W. Jiang, Y. Liu, J.T. Wang, Z. You, Y. Zhu, Critical microstructures and defects in heterostructured materials and their effects on mechanical properties, Acta Mater. 189 (2020) 129–144, https://doi.org/10.1016/j.actamat.2020.03.001.
[39] S.H. Shim, S.M. Oh, J. Lee, S.-K. Hong, S.I. Hong, Nanoscale modulated structures by balanced distribution of atoms and mechanical/structural stabilities in CoCuFeMnNi high entropy alloys, Mater. Sci. Eng. A. 762 (2019) 138120, https://doi.org/10.1016/j.msea.2019.138120.
[40] S.H. Shim, H. Pouraliakbar, H. Minouei, M.S. Rizi, V. Fallah, Y.-S. Na, J.H. Han, S. I. Hong, Characterization of the microscale/nanoscale hierarchical microstructure of an as-cast CrMnFeNiCu high-entropy alloy with promising mechanical properties, J. Alloys Compd. 954 (2023) 170091, https://doi.org/10.1016/j.jallcom.2023.170091.
[41] S.H. Shim, H. Pouraliakbar, B.J. Lee, Y.K. Kim, M.S. Rizi, S.I. Hong, Strengthening and deformation behavior of as-cast CoCrCu1.5MnNi high entropy alloy with micro-/nanoscale precipitation, Mater. Sci. Eng. A. 853 (2022) 143729, https://doi.org/10.1016/j.msea.2022.143729.
[42] R. Rawat, B.K. Singh, A. Tiwari, N. Arun, A.P. Pathak, Y. Shadangi, N. K. Mukhopadhyay, S.R. Nelamarri, S.V. Rao, A. Tripathi, Formation of Cu-Ni enriched phases during laser processing of non-equiatomic AlSiCrMnFeNiCu high entropy alloy nanoparticles, J. Alloys Compd. 927 (2022) 166905, https://doi.org/10.1016/j.jallcom.2022.166905.
[43] R. Sonkusare, P. Divya Janani, N.P. Gurao, S. Sarkar, S. Sen, K.G. Pradeep, K. Biswas, Phase equilibria in equiatomic CoCuFeMnNi high entropy alloy, Mater. Chem. Phys. 210 (2018) 269–278, https://doi.org/10.1016/j.matchemphys.2017.08.051.
[44] R. Agarwal, R. Sonkusare, S.R. Jha, N.P. Gurao, K. Biswas, N. Nayan, Understanding the deformation behavior of CoCuFeMnNi high entropy alloy by investigating mechanical properties of binary ternary and quaternary alloy subsets, Mater. Des. 157 (2018) 539–550, https://doi.org/10.1016/j.matdes.2018.07.046.
[45] B. Gwalani, D. Choudhuri, V. Soni, Y. Ren, M. Styles, J.Y. Hwang, S.J. Nam, H. Ryu, S.H. Hong, R. Banerjee, Cu assisted stabilization and nucleation of L12 precipitates in Al0.3CuFeCrNi2 fcc-based high entropy alloy, Acta Mater. 129 (2017) 170–182, https://doi.org/10.1016/j.actamat.2017.02.053.
[46] N. Jiang, H. Bian, X. Song, M. Wang, D. Lin, W. Long, S. Zhong, L. Jia, Contact-reactive brazing of CoCrFeMnNi high-entropy alloy to Zr alloys using Cu interlayer, Mater. Charact. 204 (2023) 113186, https://doi.org/10.1016/j.matchar.2023.113186.
[47] Y. Bi, Y. Xu, Z. Luo, Material characterization and mechanical performance of laser diffusion welded joint between titanium alloy and stainless steel, Mater. Lett. 336 (2023) 133927, https://doi.org/10.1016/j.matlet.2023.133927.
[48] G. Niu, Z. Zhuo, J. Mao, Inclined θ′ precipitates with terraced Cu/Mn-rich multilayers in Al–Cu alloys, J. Mater. Res. Technol. 30 (2024) 424–430, https://doi.org/10.1016/j.jmrt.2024.03.067.
[49] S.I. Hong, Criteria for predicting twin-induced plasticity in solid solution copper alloys, Mater. Sci. Eng. A. 711 (2018) 492–497, https://doi.org/10.1016/j.msea.2017.11.076.
[50] X. Liu, S. Feng, H. Xu, C. Liu, W. Zhang, H. Zhu, W. Wei, J. Kong, Achieving exceptional strength-ductility combination in a novel L12 nanoparticles-strengthened high-entropy alloy via conventional casting, Intermetallics 165 (2024) 108160, https://doi.org/10.1016/j.intermet.2023.108160.
[51] J. Apell, R. Wonneberger, M. Pügner, T. Lampke, S. Lippmann, A. Undisz, Microstructure and early-stage oxidation behavior of Co-Cr-Cu-Fe-Mn-Ni high-entropy alloys, JOM. 75 (2023) 5439–5450, https://doi.org/10.1007/s11837-023-06082-0.
[52] S.H. Shim, H. Pouraliakbar, S.I. Hong, Hierarchical structured as-cast CrFeNiMn0.5Cu0.5 high entropy alloy with excellent tensile strength/ductility properties, Scr. Mater. 210 (2022) 114473, https://doi.org/10.1016/j.scriptamat.2021.114473.
[53] L. Tang, Y. Zhou, S. Wang, N. Liang, P. Cui, N. Wang, Alloying effects on the microstructure and properties of CoCrFeMnNiX0.1 high-entropy alloys via rolling and thermal treatment, J. Mater. Sci. (2024), https://doi.org/10.1007/s10853-024-09639-9.
[54] S. Takajo, C.C. Merriman, S.C. Vogel, D.P. Field, In-situ EBSD study on the cube texture evolution in 3 wt% Si steel complemented by ex-situ EBSD experiment — From nucleation to grain growth, Acta Mater. 166 (2019) 100–112, https://doi.org/10.1016/j.actamat.2018.11.054.
[55] F. Gao, Q. Zhu, W. Xue, Y. Chen, F. Zhang, Y. Nan, S. Tang, J. Zhang, D. Tie, X. Cai, F. Yu, Z. Liu, Correlation between formability, ridging and recrystallization texture development in ferritic stainless steel fabricated by introducing intermediate annealing during cold rolling, Mater. Charact. 205 (2023) 113296, https://doi.org/10.1016/j.matchar.2023.113296.
[56] S. Paul, B. Tripathy, R. Saha, P.P. Bhattacharjee, Microstructure and texture of heavily cold-rolled and annealed extremely low stacking fault energy Cr26Mn20Fe20Co20Ni14 high entropy alloy: Comparative insights, J. Alloys Compd. 930 (2023) 167418, https://doi.org/10.1016/j.jallcom.2022.167418.
[57] J. Saha, G. Ummethala, S.R.K. Malladi, P.P. Bhattacharjee, Severe warm-rolling mediated microstructure and texture of equiatomic CoCrFeMnNi high entropy alloy: A comparison with cold-rolling, Intermetallics. 129 (2021) 107029, https://doi.org/10.1016/j.intermet.2020.107029.
[58] G.D. Sathiaraj, A. Pukenas, W. Skrotzki, Texture formation in face-centered cubic high-entropy alloys, J. Alloys Compd. 826 (2020) 154183, https://doi.org/10.1016/j.jallcom.2020.154183.
[59] Y. Chen, B. Li, B. Chen, F. Xuan, High-cycle fatigue induced twinning in CoCrFeNi high-entropy alloy processed by laser powder bed fusion additive manufacturing, Addit. Manuf. 61 (2023) 103319, https://doi.org/10.1016/j.addma.2022.103319.
[60] Z. Wu, S.A. David, D.N. Leonard, Z. Feng, H. Bei, Microstructures and mechanical properties of a welded CoCrFeMnNi high-entropy alloy, Sci. Technol. Weld. Join. 23 (2018) 585–595, https://doi.org/10.1080/13621718.2018.1430114.
[61] K. Górecki, P. Bala, G. Cios, T. Koziel, M. Stępień, K. Wieczerzak, The influence of cooling rate during crystallization on the effective partitioning coefficient in high-entropy alloys from Al-Ti-Co-Ni-Fe system, Metall. Mater. Trans. A. 47 (2016) 3257–3262, https://doi.org/10.1007/s11661-016-3498-3.

[62] S. Kumar, A. Linda, Y. Shadangi, V. Jindal, Influence of micro-segregation on the microstructure, and microhardness of MoNbTaxTi(1–x)W refractory high entropy alloys: Experimental and DFT approach, Intermetallics. 164 (2024) 108080, https://doi.org/10.1016/j.intermet.2023.108080.
[63] K. Mallieswaran, C. Rajendran, N. Aravindhan, D. Arunkumar, K. Haswanth, M. Abishek, Effect of heat treatment on the structure and properties of laser welded joints of aluminum alloy AA2024, Met. Sci. Heat Treat. 64 (2023) 564–572, https://doi.org/10.1007/s11041-023-00851-z.
[64] C. Rajendran, R. Ben Ruben, P. Ashokavarthanan, K. Mallieswaran, Identifying the Effect of PWHT on strength of laser beam welding joints of AA2024 aluminum alloy, ASME Open J. Eng. 1 (2022), https://doi.org/10.1115/1.4053496.